Development of a dynamic model of a nautical radar on a mast structure for fatigue damage analysis

Faculty of Mechanical, Maritime and Materials Engineering (3mE)

Vasileios Sfetsios

TU Delft Delft University of Technology

Rijkswaterstaat
Ministerie van Infrastructuur en Waterstaat

Development of a dynamic model of a nautical radar on a mast structure for fatigue damage analysis

by

Vasileios Sfetsios

to obtain the degree of Master of Science
at the Delft University of Technology,
to be defended publicly on June 14^{th}, 2022 at 10:00 AM.

Student number: 4999983
Project duration: February 2021 – June 2022
Thesis committee:

Dr. A. Cicirello,	TU Delft, Chair and supervisor
Dr. A. Cabboi,	TU Delft
Dr. O. J. Colomés Gené,	TU Delft
Ir. S. van Aartsen,	Rijkswaterstaat CIV

TU Delft

Rijkswaterstaat
Ministerie van Infrastructuur en Waterstaat

Abstract

Nautical radar systems are subjected to random vibrations during their service life, which may lead to the degradation of the materials and a possible fatigue failure. Assessing the impact of these vibrations to the structural integrity of the radar is crucial for drafting appropriate maintenance plans and therefore, the development of a new tool is required, which will be capable of evaluating the fatigue lifetime of the radar system.

This thesis examines a 5.7-meter-long radar antenna, supported by a lattice tower with a height of 20 meters, located in Rijkswaterstaat's test environment in Stellendam. Although the lattice structure and the radar system are coupled, they are treated separately in this study. Firstly, a Finite Element Model of the tower is developed in ANSYS, where the radar is represented by an added mass at the top floor. The aim of the model is to identify the vibrations of the structure under the influence of the incoming wind. The stochastic description of the turbulent wind is taken into account in the evaluation of the wind loads and a random vibration analysis is performed, resulting into the response of the structure in the frequency domain.

Furthermore, a second, simplified Finite Element Model of the radar system is built in ANSYS. Time series of the fluctuating wind velocity are generated and the wind load acting on the radar is approximated by the aerodynamic force in the along-wind direction, considering also the rotation of the radar antenna. In addition, the previously obtained response of the lattice structure serves as input for the radar model, representing the vibrations induced to the radar due to the motion of the structure below. The output of the model is the occurring stress response, which is subsequently used to assess the fatigue damage of the radar antenna.

The results show that the development of stresses at the bottom surface of the antenna mainly occurs at its central area. Given the assumptions used throughout the thesis, the motion of the lattice tower is found to be the governing loading condition for the resulting stresses and the magnitude of the motion significantly influences the fatigue damage of the antenna. Finally, the fatigue lifetime appears to be very sensitive to the construction materials used for the radar system. These results should be verified by future measurements in order to improve the suggested models.

Acknowledgements

This thesis marks the end of my journey in TU Delft and I would like to take this opportunity to thank several people, who contributed with their own special way to my academic and personal development.

First of all, I would like to thank my chair and daily supervisor, Dr. Alice Cicirello, for her guidance and encouragement throughout the whole duration of my thesis and for her patience to explain difficult concepts with a comprehensible and appealing approach. I am grateful for her continuous interest and desire for pushing me into improving not only my technical skills, but most importantly my critical thinking. My thanks extend to Dr. Alessandro Cabboi and Dr. Oriol Colomés Gené, for always being available and enthusiastic to discuss and show me different perspectives of my research project, which was crucial for the fulfilment of this thesis.

I would also like to express my sincerest gratitude to Simon van Aartsen for giving me the opportunity to conduct my thesis in Rijkswaterstaat and for constantly striving to support my research. His efforts to make me feel like a valuable member of the Rijkswaterstaat's team were influential for succeeding during the difficult times of the pandemic. Special thanks to the rest of the team in Rijkswaterstaat for their technical support and the constructive meetings we had.

Furthermore, I would like to thank Christos Poirazis for the endless conversations we had about the project but most importantly for the amazing experiences we are still having as friends. Many thanks to Yen-Lin Wu for his enthusiasm about exchanging views and ideas and for his help with coding challenges.

I am extremely grateful to my parents and my brother for the sacrifices they made and their unconditional support. I would also like to thank Zoe Efthymiadou for always being there for me and making me happy, no matter the situation, and for her encouragement about succeeding in my studies.

Contents

List of Figures

List of Tables

Nomenclature

Greek Symbols

χ^2	aerodynamic admittance function
Δ_σ	cycle stress range
Ω	angular velocity
ω	angular frequency [rad/sec]
ϕ_k	phase angle
ρ	air density
σ_u^2	variance of the fluctuating wind component u
σ_a	stress amplitude
σ_{max}	maximum stress
σ_{min}	minimum stress
σ_m	mean stress
σ_x	stress in the local x axis of a finite element
ζ	damping ratio
$\{\phi_i\}$	mode shape vector of mode i

Latin Symbols

A	area
c	viscous damping
C_D	drag coefficient
C_y	decay constant in the y direction
C_z	decay constant in the z direction
coh_{ij}	coherence between points i and j
D	fatigue damage
f	frequency [Hz]
F_D	drag force
H_{uF}	frequency response function
k	stiffness

L	turbulent length scale
L_t	reference length scale
m	mass
m_i	i^{th} spectral moment
N	cycles to failure
n_i	number of occurences for the stress cycle i
p_a	probability density function of the stress cycle amplitude
q	instantaneous velocity pressure
R	ratio of minimum over maximum stress
S	generic stress parameter
S_F	force spectrum
S_u	wind turbulence spectrum
S_{ij}	cross spectral density between points i and j
S_{uu}	displacement response spectrum
T	time period
T_f	fatigue lifetime
U	total wind velocity
u	fluctuating component of the wind velocity in the x axis
UX	displacement in the x axis
UY	displacement in the y axis
UZ	displacement in the z axis
v	fluctuating component of the wind velocity in the y axis
v_b	fundamental basic wind velocity
v_m	mean wind velocity
v_p	expected peak frequency
w	fluctuating component of the wind velocity in the z axis
z_0	roughness length
z_t	reference height

Acronyms

CA constant amplitude
CFD Computational Fluid Dynamics
CLD constant lifetime diagrams
DOF degrees of freedom
FEM Finite Element Model
FRF frequency response function
GFRP Glass Fiber Reinforced Polymer
MDOF multiple degrees of freedom
PDF probability density function
RPSD response power spectral density
SDOF single degree of freedom
UCS ultimate compressive strength
ULS Ultimate Limit State
UTS ultimate tensile strength
VA variable amplitude

1 Introduction

1.1. Background information

In order to collect data for the North Sea, Rijkswaterstaat, the Ministry of Infrastructure and Water Management in the Netherlands, is installing nautical radar systems on newly constructed wind farms. These systems must be able to withstand the predominant offshore conditions over their life cycle and therefore, it is essential to comprehend their structural integrity in order to assess their durability and effectiveness, achieving low maintenance costs and high availability.

The radar system under consideration consists of a long antenna, which in operational conditions, rotates with a constant angular velocity. However, during a single revolution the torque applied by the aerodynamic loads varies in time and the fluid-structure interaction between the incoming wind and the bluff body aerodynamics of the antenna heavily influences the functionality of the radar and may even result in structural failure. An example of such case occurred in 2015 at the 60 meter tall Lange Jaap lighthouse in North Holland, when the antenna that was installed at the top of the lighthouse was torn from the rest of the radar system (see Figure 1.1). The official report regarding this incident determined that the wind conditions at that time were not capable of leading to the collapse of the system. Instead, a further investigation for a possible failure due to fatigue was suggested, due to the influence of the wind fluctuations in the rotating antenna. This extreme scenario serves as additional motivation for this thesis and sets the fatigue evaluation at the center of the current research.

(a) Destroyed radar system at the lighthouse (b) Torn parts of the antenna

Figure 1.1: Lange Jaap incident

Due to the complexity of offshore operations, Rijkswaterstaat will first perform measurements in an onshore test site (Offshore Expertise Center) in Stellendam, where a mast is built with the radar system installed on its top floor (see Figure 1.2). This configuration defines the structural topology of the system under investigation in this study.

(a) Offshore Expertise Center in Stellendam (b) Antenna on the mast

Figure 1.2: Rijkswaterstaat's test environment

1.2. Problem analysis

All structural components such as buildings or sensors can be subjected to static loads but also to dynamic ones which vary with time, during their entire service life. Earthquake loads on buildings or wind acting on wind turbine generators are such examples. In order to monitor the structural health of any component, such as the nautical radar system in this case, an important task is to analyze the operational loads that act upon them and subsequently perform a fatigue damage analysis.

Vibration fatigue often deals with loads originating from environment, which are characterized by a random nature. In this study, the main source of vibrations under consideration is the wind load, which acts both in the mast and the radar itself. However, the wind velocity cannot be described by a deterministic parameter but instead it is treated as a random process. As a result, the wind load and the resulting response must be treated as well as random processes in order to be properly defined and used adequately in the vibration fatigue analysis.

Fatigue life prediction under the stochastic wind loading has been the subject of many studies. Holmes [17] investigated the use of closed-form expressions in the frequency domain in order to determine whether wind-induced fatigue needs to be taken into account in the preliminary design of structures. Jia [24] introduced a fatigue calculation based on a non-linear dynamic analysis of a flare boom structure in the time domain, while Huo and Tong [20] presented a comprehensive comparison between time domain solutions and spectral methods in the frequency domain for the estimation of the fatigue lifetime of a wind turbine tubular tower. However, for the case of a nautical radar system an existing fatigue study has not been found in literature.

In addition, a Finite Element approach for the evaluation of the wind-induced response is widely adopted in structural engineering. Wahba et al. [60] compared the use of two different types of models for the structural response of a guyed antenna mast, while Huo and Tong [21] and Ke et al. [27] developed a Finite Element Model (FEM) in order to determine the response

of a wind turbine. On the contrary, such an approach has not been investigated for a nautical radar system. The assessment of the aerodynamic loads, when the radar antenna is rotating, has been only performed with wind tunnel tests by Lombardi [31] [32] and Muggiasca et al. [38], while the latter also investigated the pressure and velocity fields around the antenna with a Computational Fluid Dynamics (CFD) analysis.

1.3. Research objective

The main objective of this research is to predict the fatigue damage of a nautical radar system by taking into account the effect of the dynamic wind load, considering also the rotation of the antenna. To this end, the development of a Finite Element Model aims to introduce a new approach that can be used in the future as a tool for the evaluation of the structural health of these systems, improving thus their maintenance plan.

Based on the above objective, the main research question of this thesis can be given as:

What could be a reliable model, which can be used to assess the fatigue damage of the nautical radar system under random vibrations?

In order to answer this question and achieve the research objective, the following sub-questions are formulated:

- How is the stochastic nature of the wind implemented in the wind loads?
- How to determine the response of the mast under the time-dependent wind fluctuations?
- How to model the effect of the wind in the rotation of the antenna?
- Which part of the radar is critical for the fatigue investigation?
- Which loading condition is governing for the response of the radar?
- Which steps are necessary for the fatigue evaluation?
- How sensitive is the fatigue damage with respect to specific parameters?
- Will it be possible to uncouple the radar from the mast?

1.4. Approach

In the research approach adopted in this thesis, the problem under consideration is divided into building blocks for the purpose of using the knowledge and existing methodologies from relevant fields.

As explained in Section 1.1, the considered structural system consists of two main components: the mast and the radar system. In order to reduce the computational time needed for the analysis [8], the two components are treated separately. Firstly, a FEM of the mast is developed in the commercial software ANSYS, while modelling choices and assumptions are defined according to existing models of similar structures. The main loading condition under investigation is the wind load that acts on the mast and therefore, a literature study is performed in order to understand the fundamentals of wind engineering, whereas the European design standard Eurocode [11] is used as additional help and guideline. The desired aim of

this FEM is to determine the wind-induced vibrations which are shared by the radar system and can be used as input for the radar model.

Subsequently, a supplementary and separate FEM is created as a representation of the nautical radar system. Due to the limited information available about the detailed construction of this system, assumptions are made and the Lange Jaap accident (see Section 1.1) has a major influence on those decisions. Furthermore, regarding the evaluation of the aerodynamic loads on the rotating antenna and taking into account the required computational power for a complete CFD analysis, a simplified approach is adopted by considering only the force in the wind flow direction.

Finally, the assessment of the fatigue damage is established based on an investigation in the available literature, with a special emphasis on composite materials. This specific selection reflects to the significant assumption of using Glass Fiber Reinforced Polymer (GFRP) as the construction material of the antenna and as a result, the wind energy sector is taken as reference due to the broad usage of composites in the production of wind turbine blades.

1.5. Thesis outline

According to the established research questions and the described methodology, the structure of this thesis is divided as follows:

- Chapter 2 aims to provide a comprehensive overview of the wind loading with a special interest for the statistical characteristics of the wind.
- Chapter 3 describes the fundamental knowledge for the fatigue life prediction of composite materials, while methods for the evaluation of the fatigue under random loads are also presented.
- Chapter 4 gives a complete elaboration of the development of the model for the mast and the determination of its response due to the influence of the stochastic wind loads.
- Chapter 5 presents the nautical radar system model, the loading conditions taken into account and the resulting fatigue assessment.
- Chapter 6 summarizes the conclusions drawn from this research and future recommendations are given.
- Appendices A - C include additional information regarding the definition of a random process, wind parameters according to Eurocode and the response of a single degree of freedom system respectively.

2

Wind modelling

Wind effects have a significant impact in the design of buildings or offshore structures. The purpose of this chapter is to provide an overview of the wind characteristics and the subsequent modelling of the wind loads, in the along-wind direction. More specifically, in Section 2.1 the nature of the wind is described. In Section 2.2, the mean wind velocity is discussed with a focus on its statistical properties, whereas Section 2.3 covers the wind fluctuations. Lastly, Section 2.4 offers a description of the wind loading in the time and frequency domains.

2.1. Nature of the wind

The basic cause of the existence of wind is the heating of the earth's surface due to solar radiation and its uneven character. Near the equator, where the sun energy is stronger, the air is heated and as a result it rises and expands, leaving low pressure zones. At the poles, the air cools and contracts, resulting into high pressure zones. These pressure differences in the earth's atmosphere produce wind flows.

The surface of the earth acts as an atmospheric boundary layer to the wind flow, introducing a frictional force that results in retardation of the flow. In addition, due to the ground roughness, pressure differences exist locally, which induce fluctuations in the wind velocity. Hence, the boundary layer is characterized by turbulence mixing. The wind zone inside this atmospheric boundary layer is of great importance in wind engineering [49].

From a mathematical point of view the instantaneous wind velocity in the boundary layer can be assumed as a composition of a mean component v_m and three perpendicular fluctuating components u, v, w. In wind engineering, one of the most significant assumptions is that the mean wind speed is steady over a short period of time. This period is usually taken as 10 min or 1 hour. In the context of this thesis, the mean wind speed is defined as the average over a period of 10 min. In the longitudinal direction, which provides the major contributions to the wind loads on a structure [10], the wind velocity is expressed as:

$$U(z,t) = v_m(z) + u(z,t) \tag{2.1}$$

The wind velocity $U(z,t)$ cannot be precisely predicted, as it varies randomly in both time and space. Hence, the wind speed and the subsequent wind loads are treated as stochastic processes and they can only be described with probability density functions (see also Appendix A). For the statistical description of the wind, it is important to distinguish between long term and short term statistics. Every 10 minutes, the mean wind speed v_m has a different value and thus it is treated as a random variable for which long term statistics can be obtained. The

fluctuating component u around the 10-min mean speed is another random variable whose properties form the short term statistics.

2.2. Mean wind speed

2.2.1. Wind shear

A typical illustration of the wind velocity profile is given in Figure 2.1. It is evident from the figure that the mean wind speed depends on the height z above the earth's surface. This is the result of the friction forces on the boundary layer, as it was mentioned in the previous section.

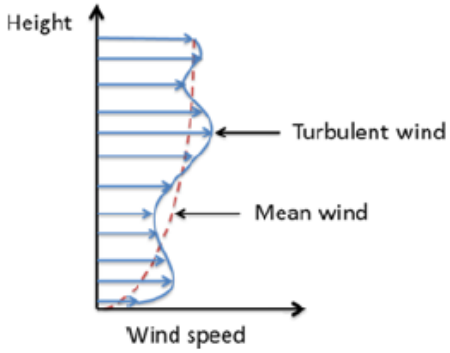

Figure 2.1: Wind velocity profile [2]

The vertical distribution of the mean wind speed is called wind shear [36] and is often described by a logarithmic law or a power law. In Eurocode [11], the mean velocity profile is given as:

$$v_m(z) = 0.19 \cdot v_b \cdot \left(\frac{z_0}{0.05}\right)^{0.07} \cdot ln\left(\frac{z}{z_0}\right), \quad if \;\; z \geq z_{min} \tag{2.2}$$

where:

v_b = fundamental basic wind velocity at 10 m above ground level [m/s] (see Section 2.2.2)

z_0 = roughness length [m]

z_{min} = minimum height below which the velocity is kept constant [m]

The roughness length z_0 is the parameter that characterizes the ground terrain and influences the vertical distribution of the mean wind speed. The reduction of the velocity nearby a flat or open area will be much less than a terrain with ground obstructions such as buildings or forests. In essence, and as it can be seen by Equation 2.2, z_0 is the height above ground at which the mean wind velocity is zero.

Information regarding the values of z_0 and z_{min} is given in Eurocode [11], and they are included in Appendix B.

2.2.2. Statistical description of the mean wind speed

For the determination of the structural loads in the design process, information about the statistical properties of the mean wind speed are necessary. As it was mentioned in Section 2.1,

the 10-min mean wind speed is variable over different time periods. This is illustrated in Figure 2.2. It has been found that a Weibull or a Rayleigh distribution represents very well the frequency of occurrence of these different 10-min wind speeds [36][50].

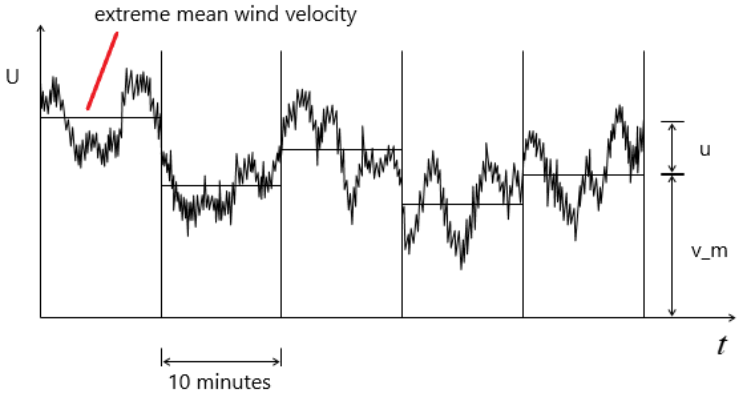

Figure 2.2: Wind velocity as a function of time. Edited figure from [59]

Another important consideration is the maximum mean wind speed over a longer period of time (see Figure 2.2). This extreme speed is very important for the design of structures, as any structure must withstand those rare but still expected events, and is usually given by design standards (such as Eurocode) depending on the criteria and limit state under consideration. The Gumbel distribution is commonly used for the statistical description of the extreme mean wind speeds.

Typically, these extreme speeds are associated with a return period. For the Ultimate Limit State (ULS) design criteria this period is often taken as 50 years. In Eurocode [11], the fundamental basic wind velocity v_b that was mentioned in Equation 2.2, is defined as the characteristic 10-min averaged mean wind velocity at 10 m above ground level, with a return period of 50 years. The fundamental basic wind velocity is representative of the climate at each site, and its value is given in the National Annex of each European country. Appendix B contains those values for the Netherlands, according to the division of the country into three areas.

An overview of the statistical distributions of the mean wind velocity is presented in Figure 2.3. The graph in the middle shows the Weibull probability density function, whereas the right one depicts the Gumbel distribution.

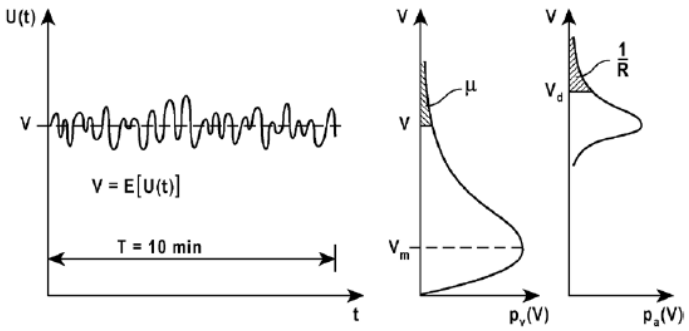

Figure 2.3: Mean wind speed statistics [50]

2.3. Wind fluctuations

2.3.1. Probability distribution

While the mean wind velocity determines the static wind load, it is the fluctuating component (turbulence) that initiates the dynamic response of the structure, resulting into vibrations. The probability distribution of the turbulent component u, within the stationary period of $T = 10$ min, is usually assumed to follow a Gaussian distribution [50] with a zero mean and variance of:

$$\sigma_u^2 = \frac{1}{T}\int_0^T u^2(t)dt \tag{2.3}$$

The fluctuations around the mean velocity and their corresponding probability distribution is illustrated in Figure 2.4.

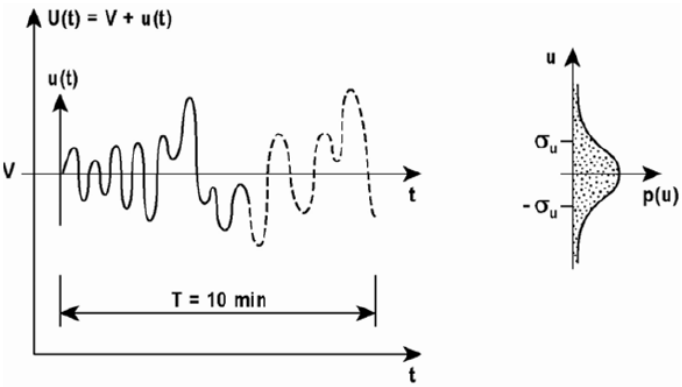

Figure 2.4: Short term statistics [50]

2.3.2. Turbulence spectrum

Van der Hoven [55] constructed a complete wind spectrum, based on full-scale measurements, which shows the distribution of turbulence energy over a wide range of frequencies. This spectrum is displayed in Figure 2.5. In structural engineering, the micro-meteorological zone is the area of interest, when determining the dynamic wind loads, due to the fact that the fundamental natural frequencies of most structures belong to that frequency range [10].

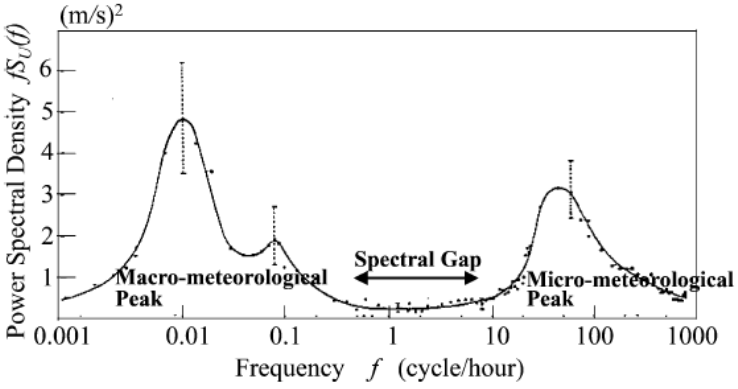

Figure 2.5: Van der Hoven wind spectrum [55]

Several formulations that describe the wind turbulence spectrum in the micro-meteorological area are given in literature, i.e. the von Karman or the Kaimal spectrum. A common characteristic of these spectra is that their right hand tail is proportional to $f^{-5/3}$, where f is the frequency in hertz. This is based on the development of smaller and smaller vortices in the higher frequencies, where their energy is dissipated as heat [3]. In the context of this thesis, the Solari spectrum is used, which is defined in Eurocode as:

$$S_u(z,f) = \frac{\sigma_u^2}{f} \cdot \frac{6.8 \cdot x(z,f)}{(1+10.2 \cdot x(z,f))^{5/3}} \tag{2.4}$$

where $x(z,f)$ is a dimensionless frequency calculated by:

$$x(z,f) = \frac{f \cdot L(z)}{v_m(z)} \tag{2.5}$$

$L(z)$ represents the turbulent length scale in meters, which can be interpreted as the average size of a wind gust in a given direction. This length scale depends on the height above ground z and on the surface roughness z_0 and is expressed as:

$$L(z) = L_t \cdot \left(\frac{z}{z_t}\right)^{\alpha} \tag{2.6}$$

where z_t is a reference height (200 m), L_t is a reference length scale (300 m) and α is given by:

$$\alpha = 0.67 + 0.05 \cdot ln(z_0) \tag{2.7}$$

An example of the Solari wind spectrum is depicted in Figure 2.6, where it is evident that in the lowest frequency range, the energy distribution of turbulence is significantly higher.

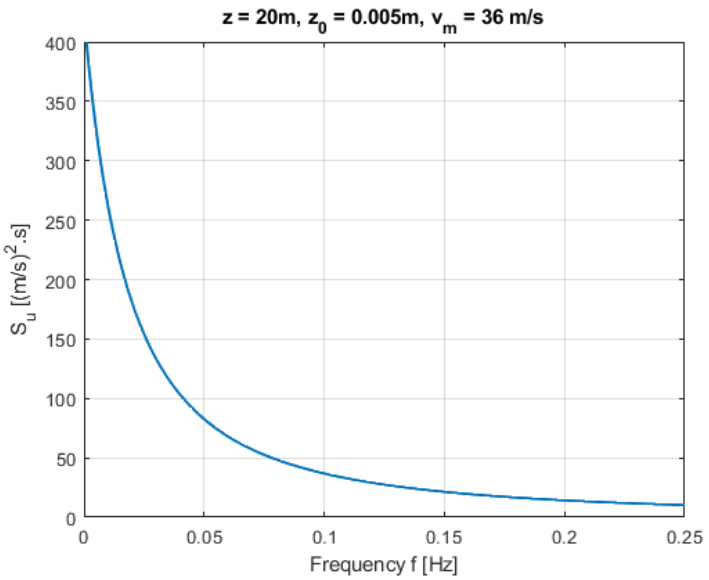

Figure 2.6: Solari wind velocity spectrum

2.3.3. Correlation between turbulence at two points

When determining the wind velocities in two different points in the wind field, it is important to take into account the spatial variation of the turbulence. For example, when a wind gust

hits the top floor of a vertical building, a lower floor might experience a similar gust or a totally different one. The same phenomenon can happen between two points of a bridge in the lateral direction. This correlation is dependent on the distance between the points and on the size of the gusts, and is expressed by a coherence function as follows [7]:

$$coh_{12}(f) = exp\left[-\frac{f \cdot \sqrt{C_z^2 \cdot (z_1 - z_2)^2 + C_y^2 \cdot (y_1 - y_2)^2}}{U_{avg}}\right] \tag{2.8}$$

where:

z, y = vertical and lateral coordinates

C_z, C_y = decay constants

U_{avg} = average mean wind velocity between points

In the above formula, the dimensions of the gusts are expressed by their frequency f. Large-size vortices have a lower frequency than small-size ones [51]. The decay parameters C_z, C_y are empirical constants determined by fitting data from measurements. Eurocode specifies both constants to be 11.5, based on the work by Solari [48].

The coherence function is illustrated in Figure 2.7 for a simple case of a vertical cantilever beam (no lateral distance). It can be seen that when the distance is small, then the turbulence components between the two points are very well correlated. In addition, the correlation is higher for smaller-size vortices than larger ones.

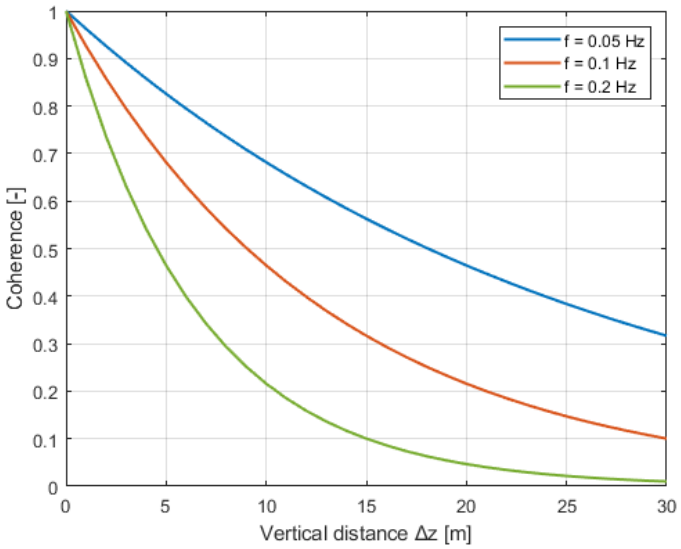

Figure 2.7: Coherence function for three different frequencies

The statistical dependence of turbulence between two points is reflected in the cross-spectral density function [23]:

$$S_{12}(f) = \sqrt{S_{11}(f) \cdot S_{22}(f)} \cdot coh_{12}(f) \tag{2.9}$$

where $S_{12}(f)$ is the cross-spectrum, $S_{ii}(f)$ is the auto-spectral density in point $i = 1, 2$ calculated by Equation 2.4 and coh_{12} is given by Equation 2.8.

2.4. Wind loading

2.4.1. Wind pressure and drag force

The basic assumption for the determination of the wind load in the along-wind direction, is that it can be calculated from the instantaneous velocity pressure which is given by the Bernoulli's equation:

$$q(t) = \frac{1}{2} \cdot \rho \cdot U^2(t) \tag{2.10}$$

where ρ is the air density and U is defined by Equation 2.1, for a specific height z.

For a small structure with area A inside the wind flow, the corresponding aerodynamic force experienced by the structure in the wind flow direction is the drag force F_D:

$$F_D(t) = \frac{1}{2} \cdot C_D \cdot \rho \cdot A \cdot U^2(t) \tag{2.11}$$

where C_D is the drag coefficient.

As it was mentioned however in Section 2.1, the wind velocity and the corresponding wind loads are random in nature, and thus are treated as stochastic processes. In order to mathematically model such a process, two different approaches can be taken; modelling in the time or frequency domain. The choice of the modelling domain depends on the problem at hand and the desired output.

2.4.2. Time domain and generation of time-series simulations

Modelling the wind velocity and load in the time domain provides the most natural representation of the wind flow. The wind velocity can be measured in a specific location by placing sensors, such as a wind anemometer. However, it is difficult to measure the velocity for a period of time that is long enough to produce reliable statistics. In addition, an analytical solution can be challenging due to the random character of the wind. The amplitude of the load at a point in time or space is eventually only one possible realization of a random variable. As a result, an ensemble of multiple realizations is needed in order to evaluate the process, which makes the analysis computationally very expensive [47]. Despite these drawbacks, modelling in the time domain can become advantageous when non-linear effects exist in the system [50] [51]. Given that real measurements of the wind velocity might not be sufficient or not available at all, artificially generated wind time-histories become necessary. For this case, Shinozuka [45] [46] proposed the harmony superposition method for the simulation of time-histories. This method is presented in the following paragraphs.

The basis for Shinozuka's method is that a stationary Gaussian process can be considered as the sum of harmonic components with random phase angle ϕ_k. When the auto-spectral density of a stationary Gaussian process is known, which in the case of wind can be obtained from design standards such as Eurocode, random time-series can be generated, with the use of an inverse Fourier transformation. This is illustrated in Figure 2.8:

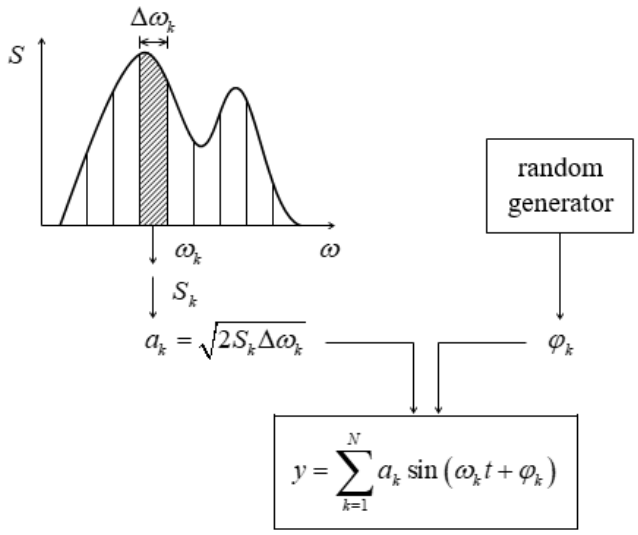

Figure 2.8: Spectral decomposition [59]

For the simulation of time-series that belong to multiple points n in the wind field, the spatial correlation between the fluctuating components must be taken into account, as it was described in Section 2.3.3. Then all the frequency and spatial information are included in the spectral density matrix $S(\omega)$, given by:

$$S(\omega) = \begin{bmatrix} S_{11}(\omega) & S_{12}(\omega) & \dots & S_{1n}(\omega) \\ S_{21}(\omega) & S_{22}(\omega) & \dots & S_{2n}(\omega) \\ \dots & \dots & \dots & \dots \\ S_{n1}(\omega) & S_{n2}(\omega) & \dots & S_{nn}(\omega) \end{bmatrix} \tag{2.12}$$

In the above equation, $S_{ii}(\omega)$ is the auto-spectral density which is calculated with Equation 2.4. It is important to note that the original spectrum depends on the frequency f (Hz), while here the angular frequency ω (rad/s) is used. The conversion between the two spectra is expressed as:

$$S_{ii}(f) \cdot \Delta f = S_{ii}(\omega) \cdot \Delta\omega = S_{ii}(\omega) \cdot (2\pi \cdot \Delta f) \Rightarrow S_{ii}(f) = 2\pi \cdot S_{ii}(\omega) \tag{2.13}$$

The elements $S_{ij}(\omega)$ are the corresponding cross spectral densities between points i and j, and they are defined with Equation 2.9, or similarly as:

$$S_{ij}(\omega) = \sqrt{S_{ii}(\omega) \cdot S_{jj}(\omega)} \cdot coh_{ij}(\omega) \tag{2.14}$$

Performing a Cholesky decomposition in the spectral density matrix $S(\omega)$, will result into a lower triangular matrix:

$$G(\omega) = \begin{bmatrix} G_{11}(\omega) & 0 & \dots & 0 \\ G_{21}(\omega) & G_{22}(\omega) & \dots & 0 \\ \dots & \dots & \dots & \dots \\ G_{n1}(\omega) & G_{n2}(\omega) & \dots & G_{nn}(\omega) \end{bmatrix} \tag{2.15}$$

which satisfies the equation:

$$S(\omega) = G(\omega) \cdot G^*(\omega)^T \tag{2.16}$$

where $G^*(\omega)$ is the complex conjugate of $G(\omega)$.

By dividing the wind spectrum into N equal frequency segments, the generated fluctuating wind speed time series at points $j = 1, 2, 3, ..., n$ are expressed as:

$$u_j(t) = \sum_{k=1}^{j} \sum_{l=1}^{N} |G_{jk}(\omega_l)| \cdot \sqrt{2\Delta\omega} \cdot cos[\omega_l \cdot t + \phi_{kl}] \tag{2.17}$$

where:

$\Delta\omega$ = frequency segment

l = 1,2,3,...,N (frequency segment number)

$G_{jk}(\omega_l)$ = element of the lower triangular matrix $G(\omega_l)$

ϕ_{kl} = random phase angle, uniformly distributed between 0 and 2π

Finally, the wind load is found with Equation 2.11, by also taking into account the mean component.

2.4.3. Frequency domain

For a given stationary Gaussian process, such as the wind fluctuations, modelling in the frequency domain can be mathematically more efficient than the time-domain. Moreover, if the system is linear, then the frequency domain provides an association with structural dynamics. More specifically, the random response of the structure (output) is directly related to the random wind load (input) through the modal properties of the structure.

The power spectral density of the fluctuating wind load at a specific height z can be derived from the wind turbulence spectrum and the drag force as [10]:

$$S_F(f) = \frac{4 \cdot \overline{F_D}^2}{{v_m}^2} \cdot S_u(f) \tag{2.18}$$

where:

$\overline{F_D}$ = mean component of the drag force (Equation 2.11)

$S_u(f)$ = wind turbulence spectrum (Equation 2.4)

v_m = mean wind velocity (Equation 2.2) at height z

However, the force acting on the structure depends on the size of the wind gust in relation to the size of the structure. This dependence basically describes the effectiveness of the structure in capturing the wind [51] and is expressed with an aerodynamic admittance function χ^2, which was empirically determined by Vickery [58] and Davenport [6] as:

$$\chi^2 = \left[\frac{1}{1 + \left(\frac{2f\sqrt{A}}{v_m} \right)^{4/3}} \right]^2 \tag{2.19}$$

where f is the gust frequency and A is the area of the structure. The aerodynamic admittance function is plotted in Figure 2.9 as a function of the term $\frac{f\sqrt{A}}{v_m}$. It is fairly obvious that for a given area A, more force is transferred to the structure for large-size vortices (low frequency) than small-size ones (high frequency).

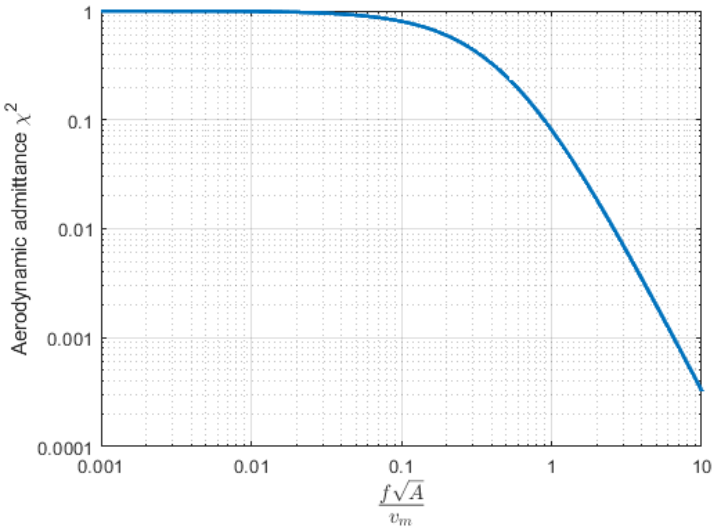

Figure 2.9: Aerodynamic admittance

Taking into account the aerodynamic admittance function, Equation 2.18 for the wind load spectrum becomes [10]:

$$S_F(f) = \frac{4 \cdot \overline{F_D}^2}{v_m^2} \cdot \chi^2 \cdot S_u(f) \tag{2.20}$$

2.5. Conclusion

The wind velocity consists of a mean and a fluctuating component and due to the random nature of wind, both components are treated as random variables. The mean wind speed varies with the height above ground, due to the development of friction in the earth's surface. During a short period of time the mean wind speed is considered to be steady and therefore, long term statistics can be obtained. On the contrary, short term statistics describe the wind fluctuations over this short period of time and the statistical information are included in the turbulence spectrum. Bernoulli's equation provides the basis for the formulation of wind loads, which can be modelled either in the time domain or the frequency domain.

3

Fatigue of composite materials

Fatigue is the phenomenon of material failure due to the initiation and propagation of cracks under the influence of cyclic loading. This chapter covers the fundamental aspects of fatigue assessment in composite materials. Section 3.1 focuses on the fatigue behaviour under the influence of loads with constant amplitude. In Section 3.2, fatigue life is described when the loading pattern is irregular. Design recommendations for the fatigue assessment are given in Section 3.3, while a probabilistic approach in the case of random fatigue is discussed in Section 3.4.

3.1. Constant amplitude loading

3.1.1. General overview

In order to determine the fatigue damage of composite materials (or steel), experiments are required. These experiments are conducted with constant amplitude (CA) loads, which are typically represented by a sinusoidal waveform. The characteristics of this waveform are given in Figure 3.1, where the vertical axis depicts the generic quantity *S*. The term *S* can indicate loads, stresses, strains or displacements which can be further categorized into amplitude, range, maximum or minimum. For the remainder of this report, the term *S* will refer specifically to stresses.

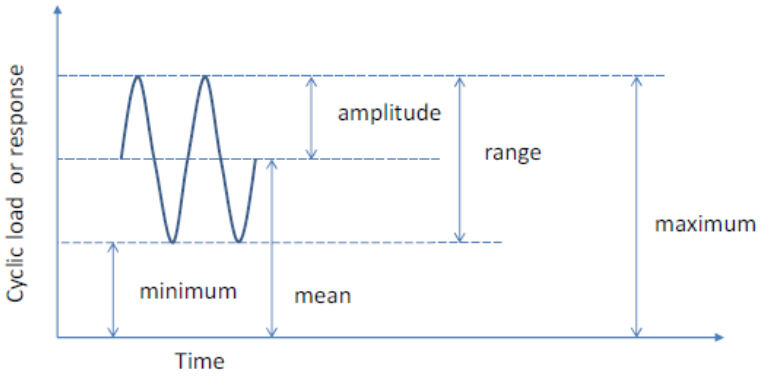

Figure 3.1: Definitions of fatigue parameters [33]

Besides the parameters that are depicted in Figure 3.1, an important quantity that also characterizes the loading conditions is the R value, which is defined as the ratio of minimum over maximum stress:

$$R = \frac{\sigma_{min}}{\sigma_{max}} \tag{3.1}$$

Depending on the R value, three general loading conditions are identified as follows:

- Tensile cyclic loading (T-T), when $0 < R < 1$
- Compressive cyclic loading (C-C), when $1 < R < +\infty$
- Tension-compression cyclic loading (T-C), when $-\infty < R < 0$

An important case occurs when $R = -1$, meaning that the minimum (compressive) stress is equal to the maximum (tensile) stress with a zero mean stress. This case is called reverse loading.

3.1.2. S-N diagrams

During experiments, for specific *S* ranges the number of cycles to failure *N* is measured, leading to the plotting of S-N diagrams with *S* on the vertical axis, whereas the horizontal axis depicts the corresponding cycles *N*. A sketch example is illustrated on Figure 3.2.

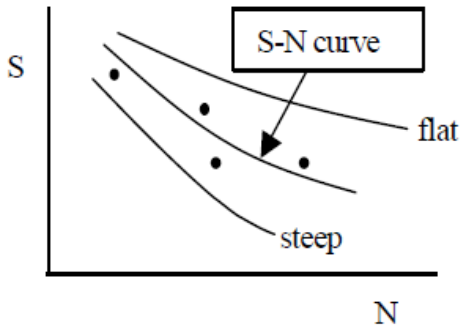

Figure 3.2: S-N diagram [40]

In general, the slope of the S-N curve characterises the fatigue resistance of the material. A ”flat” curve (small slope) indicates a better fatigue behaviour than a ”steep” curve, because a small decrease in the stress range results into a rapid increase in the number of cycles to failure. Nijssen [40] notes that composites depict a good fatigue behaviour, although a fatigue limit is absent, meaning that every stress range is damaging. On the contrary, in metals a certain limit exists, below which the fatigue life becomes infinite.

In the analytical formulations of the S-N curves, traditionally the logarithm of the cycles to failure *N* depends linearly on the stress parameter *S* or its logarithm, leading to the following expressions:

$$logN = a + b \cdot logS \tag{3.2}$$

and

$$logN = c + d \cdot S \tag{3.3}$$

where:

N = fatigue lifetime

S = generic stress parameter

$a - d$ = constants

Equation 3.2 is known as the log-log formulation and can be equivalently written in a power law formulation as:

$$N = 10^a \cdot S^b \tag{3.4}$$

The log-log (or the power law) formulation is used more often, due to higher accuracy in the extrapolation to high-cycle fatigue [25][39].

The constants a, b, c, d are determined by fitting the above mathematical formulations to the experimental data. The stress parameter *S* could refer to σ_{max} (maximum cyclic stress), σ_a (cyclic stress amplitude) or $\Delta\sigma$ (cyclic stress range). However, none of these parameters can define by themselves the constant amplitude waveform. Hence, in order for the S-N diagram to be complete, the R value is typically used as the second required parameter, resulting in different S-N curves for different R values.

3.1.3. Constant Life Diagrams

For the complete description of the fatigue behaviour of a material, a S-N diagram is not enough, since it is plotted for a unique R value. Therefore, S-N curves are required for all the other R values as well, in order to characterize a variety of loading conditions. However, a problem arises for specific loading patterns for which no experimental data exist. In order to tackle this problem, constant lifetime diagrams (CLD) were established. In essence, a CLD offers a description of the effects of the mean stress in the fatigue properties of a material, in the σ_m - σ_a space. Figure 3.3 depicts an illustrative CLD which was constructed by Philippidis and Vassilopoulos [43] .

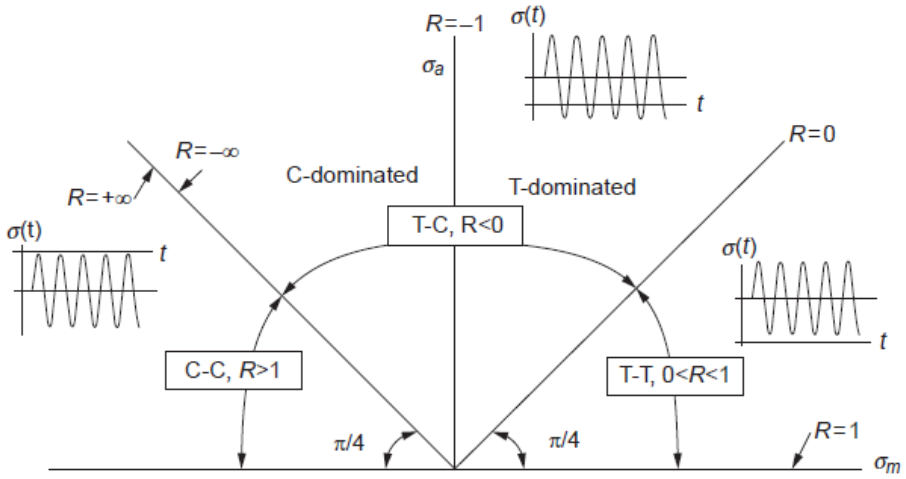

Figure 3.3: Annotation for σ_m - σ_a plane [43]

The horizontal axis of the graph represents the mean stress σ_m, whereas the vertical axis shows the stress amplitude σ_a and is co-located with the $R = -1$ line ($\sigma_m = 0$). The graph is

divided into three sections depending on the R value, as it was described in 3.1.1. Each radial line in the tension-tension (T-T) section, has a symmetric line in the compression-compression (C-C) section and the R value of each line is the inverse R value of its symmetric counterpart.

Every radial line represents a unique S-N curve, and every point of the line reflects the number of cycles to failure for the corresponding σ_a. By joining points with the same number of cycles from multiple radial lines, CLDs can be constructed.

One of the most commonly used and simple CLDs is the linear Goodman diagram (Figure 3.4), which is based on the S-N curve for the $R = -1$ value, the ultimate tensile strength (UTS) and the ultimate compressive strength (UCS). For any given combination of σ_a and σ_m, an equivalent stress amplitude σ_{eq} at $R = -1$ is obtained. Then the permissible number of cycles *N* can be calculated by any S-N formulation, e.g. using Equation 3.2.

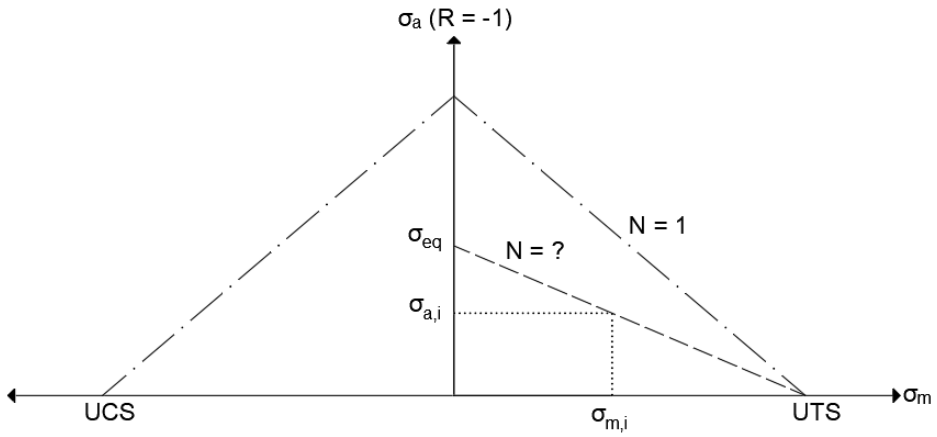

Figure 3.4: Linear Goodman diagram [40]

The linear Goodman diagram is very suitable for metals, because they present similar fatigue properties under tension or compression. However, several researchers ([14][26][35]) have identified that for composites, the linear Goodman diagram does not always provide a good fit with experimental data, because composites exhibit very different fatigue failure mechanisms in tension and compression. To account for this, a shifted version was developed, in which the top point is moved to the right (to the average between UTS and UCS), away from the $R = -1$ line.

3.2. Variable amplitude loading

3.2.1. General overview

As it was mentioned in 3.1.1, fatigue experiments are conducted with constant amplitude loads. In reality though, the load consists of cycles with different amplitudes. For the prediction of the fatigue life, these variable amplitude (VA) loads are considered to be combinations of constant amplitude loads, with the use of a counting method. For each combination, the fatigue behaviour is modelled with the determination of the S-N curve and the construction of a CLD. Finally, the damage of each combination is accumulated to a total damage, based on a summation technique. An overview of the steps required for the treatment of fatigue under variable amplitude loading is presented in Figure 3.5.

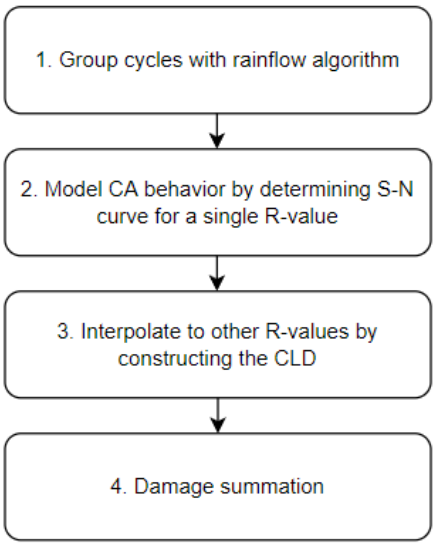

Figure 3.5: Basic steps for fatigue life prediction under VA loading

3.2.2. Counting methods

Cycle counting algorithms have been developed in order to transform irregular loading patterns into cycles of various sizes, providing also the number of their occurrences. Out of several methods that have been proposed throughout the years, the *rainflow* counting is the most commonly used counting algorithm [56], especially for composites. The reason for this is that the information of the mean stress is lost in one-parameter methods, such as the level-crossing technique. Hence, these methods are not suitable for the fatigue assessment in composite materials. A detailed description of the rainflow algorithm is given in [9]. Usually, the results of the rainflow counting are presented in a histogram plot, where each bin represents the number of occurrences (cycles) per stress range.

3.2.3. Damage summation

The final step for the fatigue life assessment is the damage accumulation of all the identified cycles. One of the most popular and established tools for calculating the damage contribution of each cycle is the linear Palmgren-Miner rule [37][41]. Each stress cycle is associated directly with the S-N equation, resulting into the permissible number of cycles N_i. By dividing the number of occurences n_i, that has been identified through the rainflow algorithm for each stress cycle, with N_i, an incremental damage coefficient is calculated. Summing up all the individual damage coefficients, the total damage D is found. According to the rule, the material does not fail when the total damage is less than 1. The following equation describes the linear Palmgren-Miner sum:

$$D = \sum_i \frac{n_i}{N_i} < 1 \tag{3.5}$$

The use of linear Palmgren-Miner rule in the fatigue assessment does not always produce accurate results [56], because of its limitations. Firstly, the definition of failure is arbitrary and as a result a large scatter in the failure states has been observed [40]. Secondly, load sequence effects are completely overlooked, whereas experiments have shown that the damage caused by a cycle is in fact dependent on the damage state prior to this cycle [16]. Despite these draw-

backs, Equation 3.5 is preferred in engineering practice and it is adopted in design standards due to its simplicity.

3.3. Fatigue regulations according to Germanischer Lloyd

Guideline for the Certification of Offshore Wind Turbines [15] applies to the design, approval and certification of wind turbines. This document includes a detailed fatigue analysis of GFRP components.

The fatigue lifetime is determined according to the shifted Goodman diagram that is described in Section 3.1.3. When a unique S-N curve exists for the specific material under consideration, then the Goodman diagram is constructed using this curve. Otherwise, a simplified assumption for the slope parameter m of the S-N curve is used. The permissible number of cycles are calculated from the Goodman diagram with the following equation:

$$N = \left[\frac{R_{k,t} + |R_{k,c}| - |2 \cdot \gamma_{Ma} \cdot S_{k,M} - R_{k,t} + |R_{k,c}||}{2 \cdot (\gamma_{Mb}/C_{1b}) \cdot S_{k,A}} \right]^m \tag{3.6}$$

where:

$S_{k,M}$ = mean value of characteristic actions

$S_{k,A}$ = amplitude of characteristic actions

$R_{k,t}$ = characteristic short-term structural member resistance for tension

$R_{k,c}$ = characteristic short-term structural member resistance for compression

m = slope parameter m of the S-N curve

N = permissible load cycle number

γ_{Ma} = partial safety factor for the material (short-term strength)

γ_{Mb} = partial safety factor for the material (fatigue strength)

C_{1b} = $N^{1/m}$ curve of high-cycle fatigue for the load cycle number N and slope parameter m.

Finally, the fatigue assessment is based on the Palmgren-Miner sum, as it is provided in Equation 3.5.

It is important to note however, that the above design criteria disregard completely the multiaxial development of stresses, which is the case in an actual structure. Instead, as a simplification, they consider only the uniaxial stress state in the material, resulting into high safety factors [42].

3.4. Probabilistic approach

The fatigue assessment methodology that is described in the previous sections concerns situations where the loads and the corresponding stresses are deterministic. However, as it was explained in Chapter 2, wind loads have a random nature and they are treated as stochastic processes. Therefore, the resulting stresses and the identified rainflow cycles are not discrete but instead they are characterized by a probability distribution. This is illustrated in Figure 3.6, where the upper example shows the (discrete) rainflow histogram bins under a deterministic load. On the contrary, the lower example corresponds to a random loading case where the rainflow amplitude is now described with a continuous probability density function (PDF).

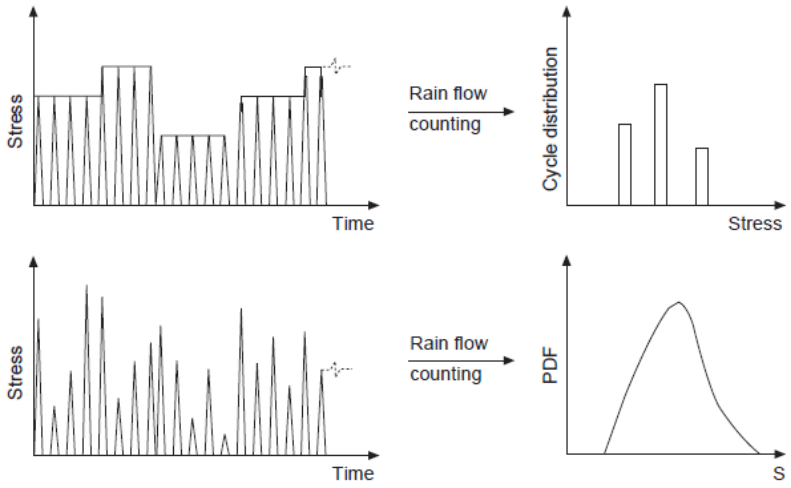

Figure 3.6: Cycle distribution with rainflow method [30]

3.4.1. Time domain

In the wind energy field, the evaluation of random fatigue loads is traditionally performed in the time domain using different time histories of the wind turbulence, i.e. different turbulence seed values [53]. For each simulation i, the fatigue damage is assessed with the steps described in Figure 3.5 and the expected fatigue damage is obtained as the average damage over the simulations M [19]:

$$D_e = \frac{1}{M} \sum_{i=1}^{M} D_i \tag{3.7}$$

Analyzing the fatigue in the time domain is considered to be highly accurate and is independent of the probability distribution of the random stress, although it requires a large amount of calculations, which makes the procedure time consuming and therefore it is not always convenient for practical applications.

3.4.2. Frequency domain and spectral moments methods

In order to improve the calculation time, random fatigue can be evaluated in the frequency domain. The key factor in this approach is the determination of the cycle amplitude PDF [47], as shown in the lower side of Figure 3.6. Then the damage summation (Equation 3.5) over a period of time T can be described with an integral as [47]:

$$D = \nu_p \cdot C^{-1} \cdot T \cdot \int_0^\infty S^k \cdot p_a(S) dS \tag{3.8}$$

where $C = 10^a$ and $k = -b$ from the power law formulation (Equation 3.4), p_a is the cycle amplitude PDF and ν_p is the expected peak frequency (in hertz), which in the case of a stationary Gaussian process is given as [47]:

$$\nu_p = \frac{1}{2\pi}\sqrt{\frac{m_4}{m_2}} \tag{3.9}$$

where m_i $(i = 2, 4)$ is the ith spectral moment of a power spectral density $S_{xx}(\omega)$:

$$m_i = \int_{-\infty}^{\infty} \omega^i \cdot S_{xx}(\omega) d\omega \tag{3.10}$$

The peak frequency ν_p is found with a level (threshold) crossing analysis and describes the expected number of peaks per unit time. For further elaboration on the level crossing method, the reader is referred to [29].

The fatigue life can be calculated with Equation 3.8, by setting $D = 1$ and thus resulting in the time-to-failure $T = T_f$. The only unknown is the PDF of the cycle amplitude p_a. This can be estimated using empirical models based on simulations, known as the spectral moments methods. The most common approaches are given in Table 3.1, while a comprehensive description of the methods can be found in [47].

Table 3.1: Spectral moments methods depending on the bandwidth of the stress spectrum

Narrowband spectrum	**Broadband spectrum**
Narrowband approximation	Wirsching-Light
	Dirlik
	Zhao-Baker
	$\alpha_{0.75}$

The major advantage of the use of spectral moments methods in the frequency domain is that fatigue results can be obtained with a very efficient numerical analysis. However, this approach is relied upon the assumption that the random stress is a stationary Gaussian process, which limits its applicability. Despite this simplification, the obtained results can be used as a first estimate, for example in the preliminary design stage, in order to determine if fatigue under wind loading is likely to occur [17] [20].

An overview of the steps required for the assessment of the fatigue induced by random wind loading is shown in Figure 3.7:

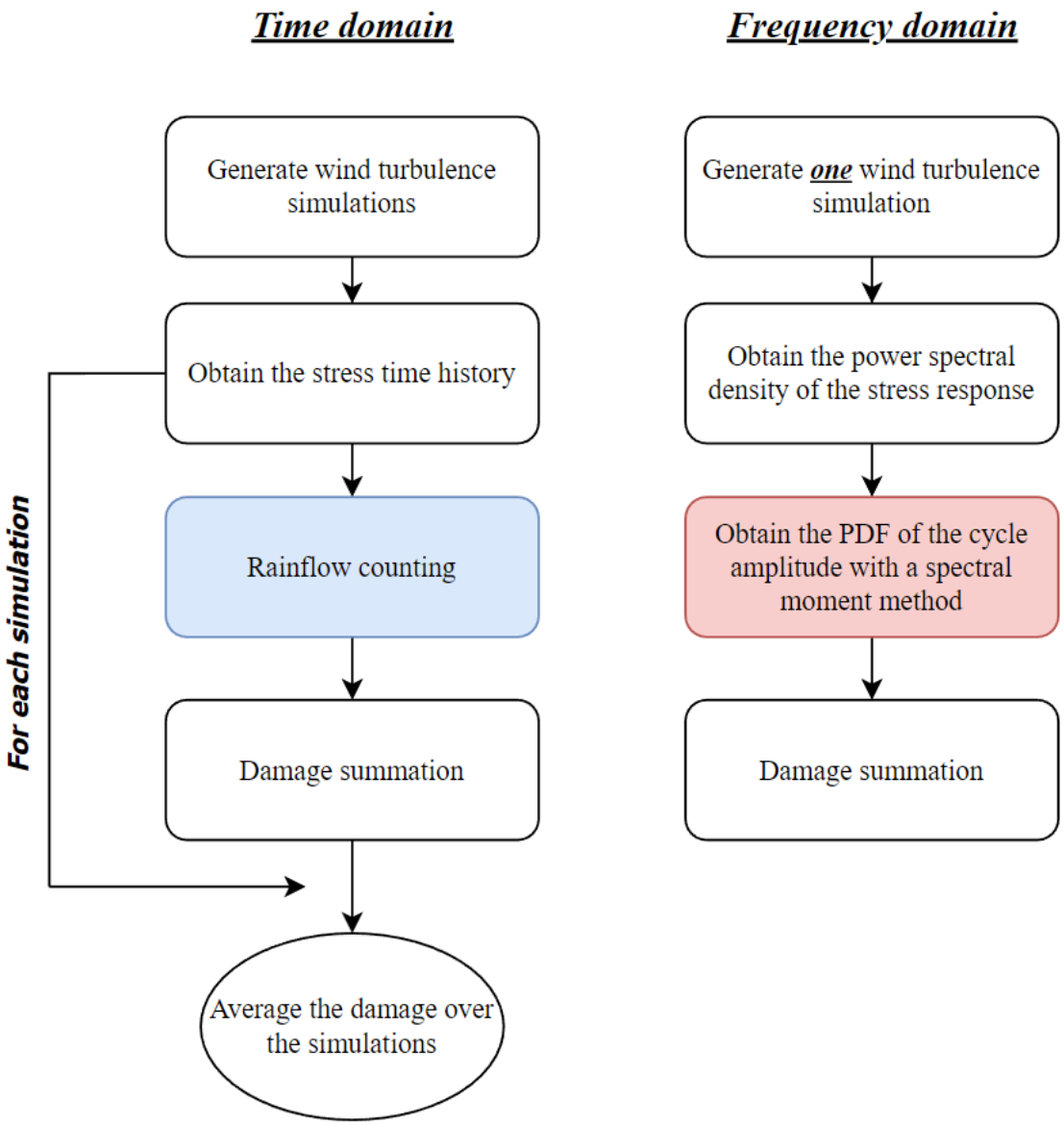

Figure 3.7: Basic steps for the fatigue evaluation under random wind loads

3.5. Conclusion

Constant amplitude fatigue provides the basis for fatigue predictions of composite materials under realistic conditions. Analytical expressions for the S-N curves are described, from which the number of cycles to failure can be found, depending on the applied load. Using constant lifetime diagrams, the fatigue properties of a material are evaluated under the full loading spectrum. Variable amplitude loads are treated as combinations of multiple constant amplitude loads, using the rainflow counting method. Every unique constant amplitude cycle contributes to the damage of the material and the structural integrity is assessed by summing up all the damage contributions. Design recommendations for wind turbines provide an elaborated fatigue assessment for composites, although they disregard the occurrence of complex stress states. In the case of wind loads, the resulting random fatigue can be evaluated either in the time domain with multiple simulations or in the frequency domain with the use of spectral moments methods.

4

Mast model & wind-induced vibrations

As the radar is mounted on the top floor of the lattice tower, it shares the vibrations that this structure experiences. This chapter describes the development of a FEM in the commercial software ANSYS, that can determine the structural response of the lattice tower under the stochastic wind excitation. In Section 4.1, details regarding the considered structure are given and also the modelling assumptions are discussed. The dynamic behaviour of the structure is evaluated with a modal analysis in Section 4.2. Finally, in Section 4.3 the response of the structure is assessed through a random vibration analysis.

4.1. Mast Finite Element Model

4.1.1. Description of the reference structure

The structure under consideration in this analysis is the antenna mast that is placed in the Offshore Expertise Center in Stellendam (see Figure 4.1a). The height of this lattice tower is 20.01 m and it consists of 7 bays, with supporting diagonal braces (see Figure 4.1b). Simplified sketch drawings of the top view and its main dimensions are given in Figure 4.2. The first five floors (Figure 4.2a) form an isosceles triangle while the upper two floors (Figure 4.2b) retain this shape but with the addition of an access platform. Each floor includes internal horizontal beams (dashed lines) as supporting members.

(a) Antenna mast in Stellendam

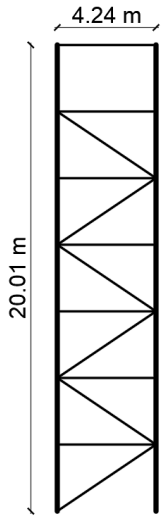

(b) Back view (simplified illustration)

Figure 4.1: Side views of the structure under consideration

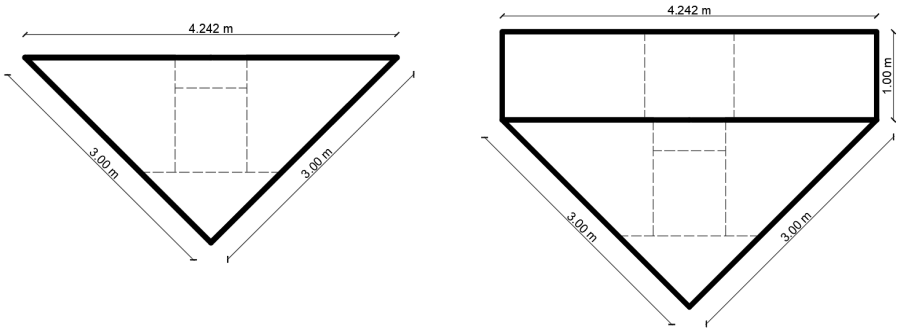

(a) First five floors (b) Upper two floors

Figure 4.2: Cross section/top view of the tower (simplified illustration)

The main structural elements are the columns, the diagonal braces and the horizontal members, while their cross sections vary from H (HEA) and U sections (UPN) to circular (CHS) ones (see Table 4.1) . These cross sections are illustrated in Figure 4.3.

Table 4.1: Structural elements and their corresponding cross sections

Element	Cross-section type
Columns	CHS
Diagonal braces	CHS
Horizontal braces	HEA or UPN

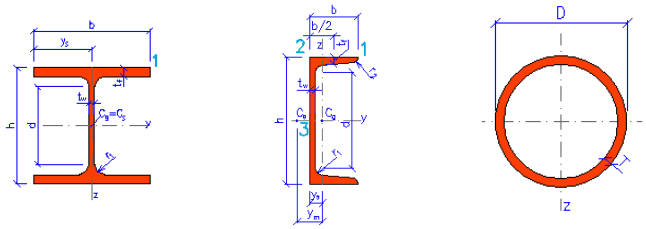

(a) HEA (b) UPN (c) CHS

Figure 4.3: Cross sections of the structural components

4.1.2. Element type

For the development of a FEM of the structure, the commercial software ANSYS is used. The model is constructed with the three main components that were mentioned in the previous section, whereas secondary details such as handrails or ladders are not included. The beam element type is chosen for the representation of the main components, since it characterizes relatively long and thin structural members and results in a realistic behaviour of framed structures [44], such as the lattice tower under consideration. This element type is based on the Timoshenko beam theory which includes shear-deformation effects. In the 3-D space, the beam element consists of two nodes and each node has six degrees of freedom (DOF). More specifically, these DOF are the translations in the x,y,z directions and the rotations about those axes, as illustrated in Figure 4.4.

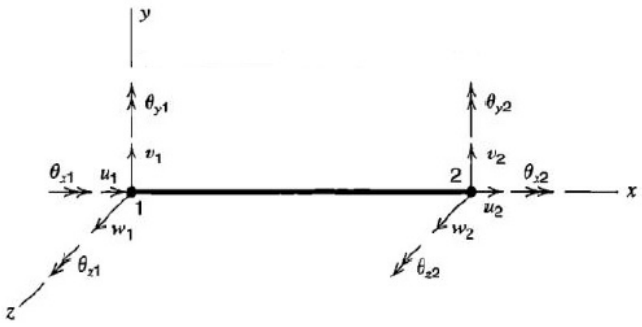

Figure 4.4: Degrees of freedom of a beam element [5]

4.1.3. Material properties and modelling assumptions

The geometry of the tower and the cross sections of the structural members, as described in 4.1.1, were the only details available regarding the structure. Therefore, in order to build a model that is as realistic as possible but also accounts for this lack of information, assumptions and simplifications were made. While it was clear that steel was used for the construction of the lattice tower, the specific steel grade was unknown and thus typical values for the material properties are assigned in the model, as presented in Table 4.2. A damping ratio of 2 % is assumed for the structure, based on recommended values for steel structures [34].

Table 4.2: Material properties of the structure

Material property	Value
Density $[kg/m^3]$	7850
Young's modulus $[GPa]$	210
Poisson's ratio [-]	0.3

Regarding the joint connection at the nodes, in the existing structure all members are welded (see Figure 4.5a). Therefore, in the FEM, the braces are considered fixed at the columns. In a real welded connection, because of manufacturing methods the weld toes of the braces are separated by a gap (see Figure 4.5b), which affects the distribution of moments and axial forces at the nodes. In this thesis, every member is attached on the same node and the gap is omitted, which is usually the case in common practice [1].

(a) Welding between members in the mast

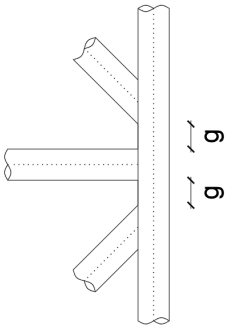

(b) Gap between weld toes

Figure 4.5: Welded connection

As it was mentioned in the previous section, secondary components such as ladders are not modelled. Instead, the density of the steel is increased by 1 %, in order to account for the mass of these neglected components. In addition, a point mass of 560 kg is attached at the top floor, which represents the radar and its supporting pedestal. This modelling decision is very important, as it implies that the radar system is assumed to be a rigid object, linked with the tower through a rigid connection, disregarding thus any (local) flexible behaviour of the radar system. Furthermore, in the existing structure each floor of the tower consists of a steel grating that acts as footing for human access (see Figure 4.6). This grating is not included explicitly in the model, but it is taken into account by treating it as a plate and distributing its weight into the supporting horizontal beams. As a result, the density of the beams that are depicted in Figure 4.2 are increased accordingly. On the other hand, the influence of the grating in the torsional stiffness of the structure is neglected, as this investigation is deemed out of the scope of this thesis.

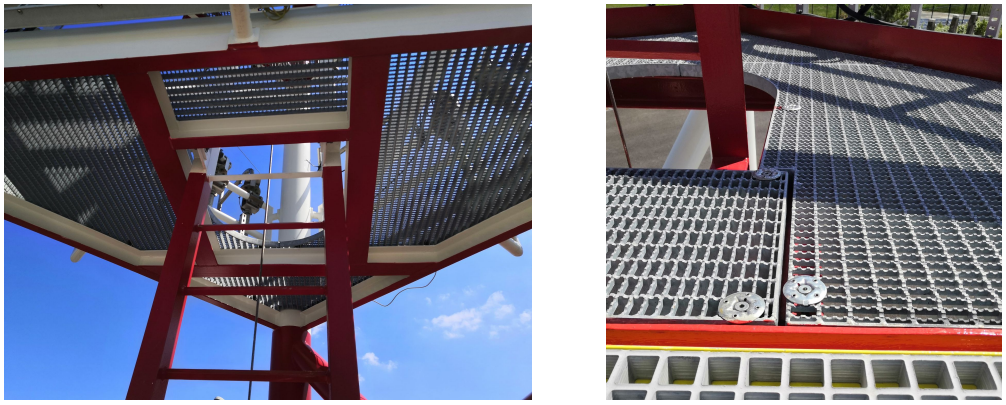

(a) Bottom view of the floor

(b) Density of the grating

Figure 4.6: Floor grating as access platform

Last but not least, the boundary conditions of the model are considered. In reality, the bases of the columns are mounted upon a concrete slab as shown in Figure 4.7. In the model, a clamped boundary is adopted for the three columns of the structure and thus all DOF at the bottom nodes of the columns are restricted, which is an important assumption as the flexibility of the soil-structure interaction is represented by a rigid boundary, resulting into an overestimation of the stiffness of the structure.

Figure 4.7: Base of the column

Based on the aforementioned assumptions a reference model is created in ANSYS, whose geometry is depicted in Figure 4.8.

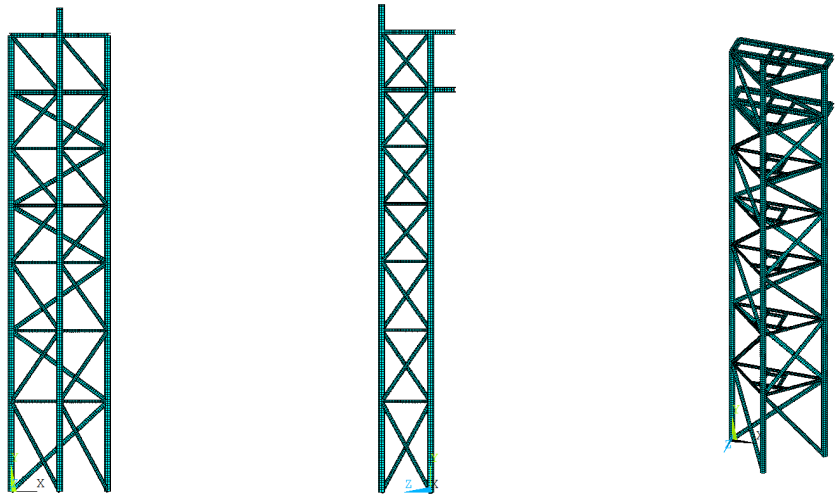

(a) Front view (b) Side view (c) 3D view

Figure 4.8: FEM geometry in ANSYS

4.2. Modal Analysis

4.2.1. Theoretical background

In structural dynamics, the natural frequencies and mode shapes are important parameters for the assessment of the dynamic behaviour of a structure and the determination of its response. Both parameters are intrinsic building properties of the structure and are independent of the loading conditions. In the following paragraphs a brief theoretical overview of these parameters is given, while the book of Chopra [4] is recommended for a more elaborate reading.

The natural frequencies or eigenfrequencies describe the frequencies at which the structure vibrates when moved from its initial (resting) position and left free. If the frequency of the external loading is close to one of the natural frequencies, then resonance may occur and the response will be amplified, resulting into excessive deformation. In the case of a single degree of freedom (SDOF) system the natural frequency depends on the mass m and stiffness k of the system, and it can be found as:

$$\omega_n = \sqrt{\frac{k}{m}} \tag{4.1}$$

A mode shape describes the deformation of a structure when it vibrates at the natural frequency. In the case of a multiple degrees of freedom (MDOF) system the mode shapes (and the natural frequencies) are determined from a modal analysis. The fundamental equation solved in an undamped modal analysis is the eigenvalue problem:

$$[K]\{\phi_i\} = \omega_i^2 [M]\{\phi_i\} \tag{4.2}$$

where:

[K] = stiffness matrix

[M] = mass matrix

ω_i = natural frequency of mode i (ω_i^2 is the eigenvalue)

$\{\phi_i\}$ = mode shape vector (eigenvector) of mode i

A modal analysis also serves as a starting point for the determination of the structural response. In a MDOF system the response can not be found analytically, because the equations of motions are coupled. However, by performing a modal analysis they can be uncoupled using the orthogonality properties of the mode shapes. As a result, the response of each mode can be solved individually similarly to a SDOF system. Finally, the total response of the structure is calculated by adding the individual modal solutions (responses).

4.2.2. Results in ANSYS

In order to investigate the dynamic behaviour of the structure and determine its natural frequencies and mode shapes, a modal analysis is performed. The resulting first three natural frequencies are shown in Table 4.3 whereas Figure 4.9 illustrates the corresponding mode shapes. In the first mode shape the structure bends about the x-axis, while in the second one it bends about the y-axis. In addition, the second mode includes a small torsional deformation, which can be explained by the asymmetry of the tower's cross section. Finally, the third natural frequency corresponds to the torsional vibration.

Table 4.3: First three natural frequencies of the mast

Mode No.	Freq. (Hz)
1	2.8726
2	4.4143
3	6.9911

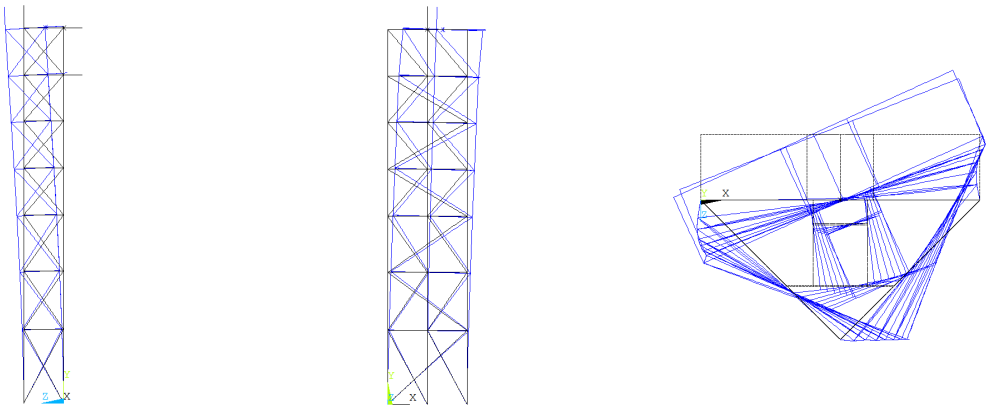

(a) First mode shape (b) Second mode shape (c) Third mode shape

Figure 4.9: Mode shapes of the mast

The influence of the mesh density on the natural frequencies is evaluated with a convergence study. The element size is chosen with respect to the column thickness $t = 8$ mm. As it

can be seen from Table 4.4, only the higher modes are affected and the difference is in the order of 1 mHz. Hence, it can be concluded that the mesh density has a limited effect on the natural frequencies and thus an element size of $10t$ is chosen as optimal, based also on the computational efficiency.

Table 4.4: Influence of the element size on the natural frequencies

Element size	100t	50t	30t	20t	10t	5t	t
Mode No.	Nat. Freq. (Hz)						
1	2.872	2.872	2.872	2.872	2.872	2.872	2.872
2	4.414	4.414	4.414	4.414	4.414	4.414	4.414
3	6.991	6.991	6.991	6.991	6.991	6.991	6.991
4	13.079	13.079	13.079	13.079	13.079	13.079	13.079
5	13.751	13.751	13.751	13.751	13.751	13.751	13.751
6	19.310	19.310	19.310	19.310	19.310	19.310	19.310
7	22.986	22.985	22.985	22.985	22.985	22.985	22.985
8	23.975	23.974	23.974	23.974	23.974	23.974	23.974
9	24.518	24.517	24.516	24.516	24.516	24.516	24.516
10	24.970	24.966	24.965	24.965	24.965	24.965	24.965

4.3. Wind-induced vibrations of the mast

4.3.1. Theoretical background

In order to determine the mast response under the influence of the stochastic wind, a random vibration analysis is needed. The analysis is performed in the frequency domain and it depends upon the fact that the random wind loading can be considered as a summation of infinite harmonic components. Chapter 2 serves as the building block for modelling the random wind load in the along-wind direction. In addition, the determination of the response in a MDOF system such as the developed FEM, is based upon the response of a SDOF system under stochastic excitation. For this reason, a brief but fundamental background regarding the response of a SDOF system due to a stationary Gaussian process is given in Appendix C.

Modelling the dynamic excitation is one of the most crucial steps for the determination of the structural response with a random vibration analysis in the frequency domain. The random excitation due to wind is described with its power spectral density as explained in Chapter 2. However, equally important and necessary is the identification of the structural properties and more specifically the deduction of the so-called frequency response function (FRF). This function which is also called the mechanical admittance in wind engineering, directly relates the amplitude of the output (response) with the amplitude of the input (load) in a linear system.

In a SDOF system, the FRF is complex and is found as:

$$H_{uF}(\omega) = \frac{1}{k - m\omega^2 + i\omega c} \tag{4.3}$$

where k is the stiffness, m is the mass and c is the viscous damping. The absolute value of the function is:

$$|H_{uF}(\omega)| = \sqrt{H_{uF}(\omega)H^*_{uF}(\omega)} = \frac{1}{\sqrt{(k - m\omega^2)^2 + (\omega c)^2}} \tag{4.4}$$

where $H^*_{uF}(\omega)$ is the complex conjugate of the FRF.

Using Equation 4.1 and the damping ratio $\zeta = c/2\sqrt{km}$, Equation 4.4 becomes:

$$|H_{uF}(\omega)| = \frac{1}{k\sqrt{(1 - (\omega/\omega_n)^2)^2 + (2\zeta(\omega/\omega_n))^2}} \tag{4.5}$$

Finally, if $S_{FF}(\omega)$ is the loading spectrum, then the response spectrum is found as (see also Appendix C):

$$S_{uu}(\omega) = |H(\omega)|^2 S_{FF}(\omega) \tag{4.6}$$

In the case of a MDOF system, the FRF can be determined with a modal analysis and describes the relationship between the response of the lth degree of freedom and the excitation applied on the ith degree of freedom [49] [59]:

$$H_{u_l F_i} = \sum_k \frac{\phi_{k,l}\phi_{k,i}}{k_k(1 - \omega^2/\omega_k^2 + 2i\zeta\omega/\omega_k)} \tag{4.7}$$

where $\phi_{k,l}, \phi_{k,i}$ are the l^{th} and i^{th} components of the k^{th} mode shape.

Analogously to Equation 4.6, the spectral response of the l^{th} degree of freedom in a MDOF system with n degrees of freedom, is calculated by:

$$S_{u_l u_l} = \sum_i^n \sum_j^n H_{u_l F_i} H^*_{u_l F_j} S_{F_i F_j} \tag{4.8}$$

where $S_{F_i F_j}$ describes the cross spectral terms that are discussed in Chapter 2.

An overview of the procedure for the calculation of the wind-induced response of a structure is illustrated in Figure 4.10. Firstly, in order to obtain the wind load spectrum, the turbulence spectrum is multiplied with the aerodynamic admittance, as explained in Section 2.4.3. The resulting response is then determined by multiplying the wind load spectrum with the structure's FRF.

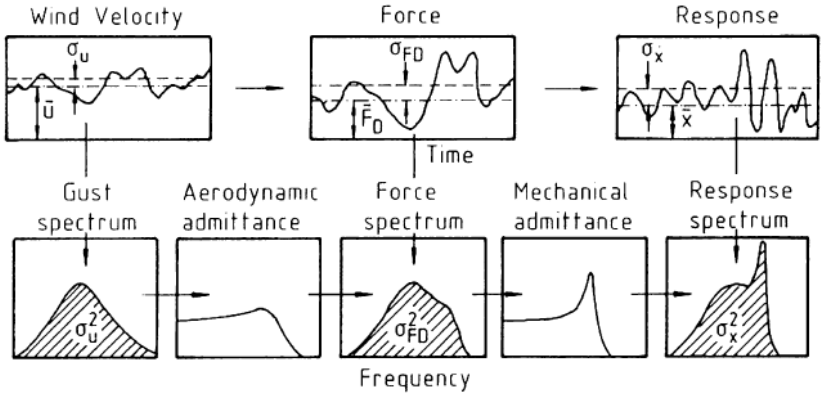

Figure 4.10: Along-wind excitation and response procedure [6]

As it can be seen from Figure 4.11, the area of the response spectrum can be divided into two parts: the background response A_B and the resonant response A_R. The background response ignores the dynamic behaviour of the structure and is the direct result of the wind load in very low frequencies. On the contrary, loading components with a frequency close to the natural frequency of the structure lead to the dynamic resonant part, which is determined from the dynamic properties of the structure through the mechanical admittance function.

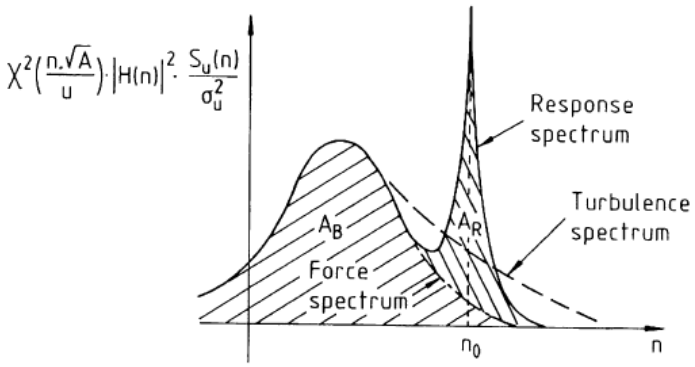

Figure 4.11: Composition of the response spectrum [49]

4.3.2. Random vibration analysis in ANSYS

Based on the brief background that is described in the previous section, a random vibration analysis is performed in ANSYS.

In order to identify the most severe wind load effect in the mast, three different wind directions are investigated in accordance with the specifications of Eurocode [12]. The considered directions are shown in Figure 4.12.

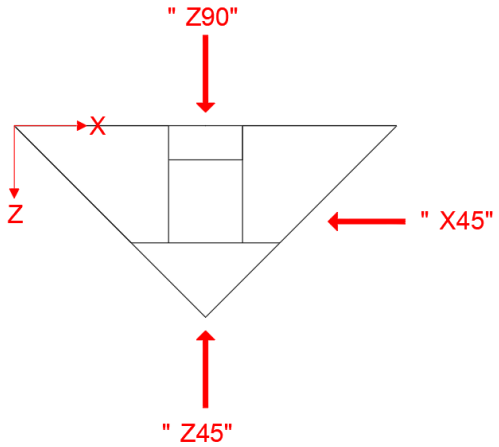

Figure 4.12: Top view of the mast and the considered wind directions

The wind load spectrum is calculated according to the theory provided in Chapter 2. For the estimation of the mean wind velocity, the ULS design criteria are taking into consideration and thus, a fundamental basic wind velocity $v_b = 27$ m/s is defined, while the roughness length z_0 = 0.2 m serves as the input parameter. Both these values are obtained from the Dutch National Annex of Eurocode [13] (see also Appendix B), based on the location of Stellendam.

In addition, the values for the drag coefficient C_D (see Equation 2.11) are defined according to Table 4.5:

Table 4.5: Drag coefficient depending on the cross-section type [12]

Cross-section type	Drag coefficient C_D
CHS	1.2
HEA	2.0
UPN	2.0

Regarding the nodal application of the spectral loads in the developed FEM, it is important to note that the drag force given in Equation 2.11 describes a point load with dimensions of $[N]$. Hence, the resulting spectral loads are actually point loads with dimensions $[N^2/Hz]$. In order to calculate these spectral loads, the loading area of the structural members needs to be defined and thus a discretization of the members is needed. In this case, the discretization does not refer to the mesh size in the FEM, but instead it concerns a division of the structure into members with an "artificial" length dL, specifying thus the loading. The initial discretization of the model and the application of the loads are illustrated in Figure 4.13 and are defined as follows:

- For the columns the segment dL covers the height of each frame of the tower and the loads are applied at the middle of each frame (Figure 4.13a).
- For the diagonal braces and the horizontal beams, dL concerns the whole length of each member and the loads are applied at the middle (Figure 4.13b and Figure 4.13c respectively).

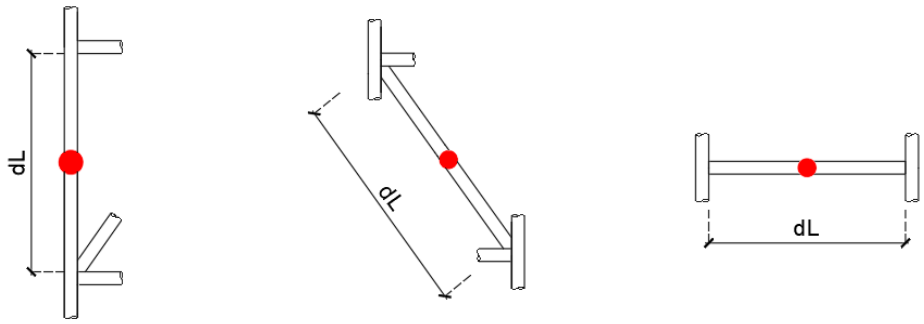

(a) dL for the columns (b) dL for the diagonal braces (c) dL for the horizontal beams

Figure 4.13: Application of the spectral point loads

4.3.3. Results

The desired output of the performed random vibration analysis is the displacement of the top floor, where the radar is placed. This displacement will be used as input for the radar modelling in Chapter 5.

As it was mentioned in Section 4.1.3, the developed FEM includes a point mass that represents the radar and the supporting pedestal. Hence, the point of interest regarding the determination of the structure's response is the specific node of the top floor, where the representation of the radar is attached. The results of the random vibration analysis for the considered wind directions are depicted in Figures 4.14 - 4.16.

Figure 4.14 shows the response power spectral density (RPSD) of the top floor's displacement in the Z axis, for the wind direction $Z45$. As it can be seen from the graph, there are two visible peaks: one in the very low frequency area and the other close to the 1^{st} natural frequency ($f_1 = 2.8726$ Hz) of the structure. As explained in 4.3.1, the first peak corresponds to the background response due to the wind load whereas the second peak is the result of the mast's mechanical admittance function.

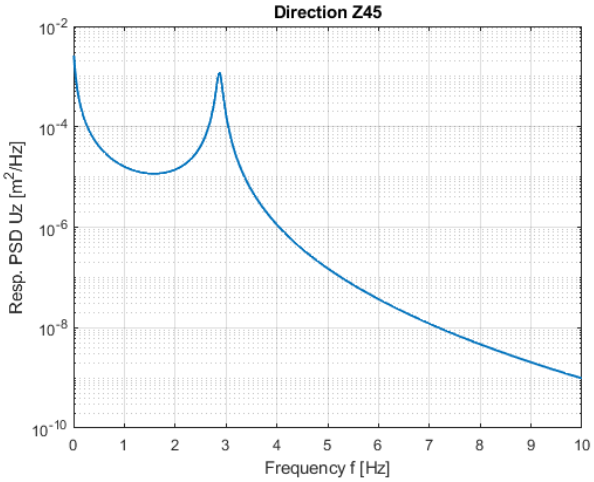

Figure 4.14: Displacement of the top floor in the Z axis for excitation in the direction $Z45$

Similarly, the resulting RPSD for the wind direction $Z90$ is given in Figure 4.15. The graph is exactly the same with the respective one for the direction $Z45$, which can be explained by the fact that the total projected area that is loaded is the same for both wind directions.

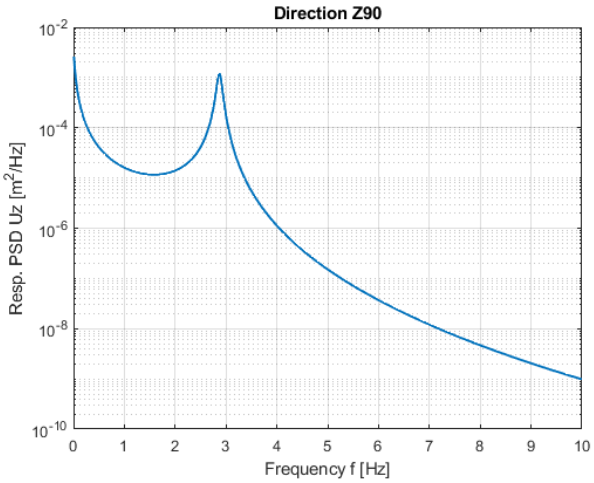

Figure 4.15: Displacement of the top floor in the Z axis for excitation in the direction $Z90$

Regarding the wind direction $X45$, the displacement of the top floor in the X axis is depicted

in Figure 4.16. In this case, three peaks are distinguished. The first one is the result of the wind load and the second one is close to the 2^{nd} natural frequency ($f_2 = 4.4143$ Hz). However, it appears that the 3^{rd} mode shape also affects the response due to the excitation in this direction. This is visible in the final peak, which is close to the 3^{rd} natural frequency ($f_3 = 6.9911$ Hz).

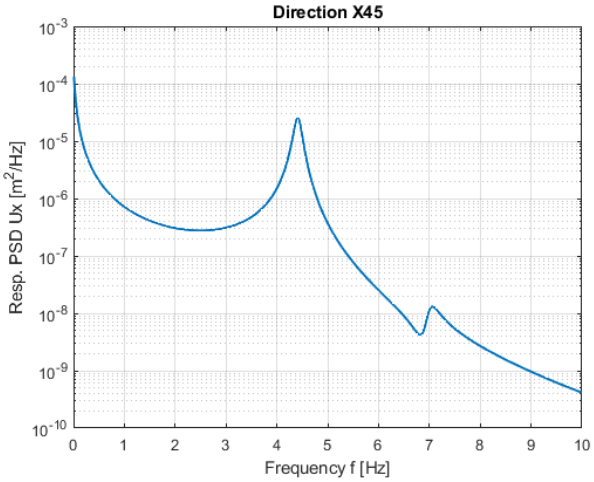

Figure 4.16: Displacement of the top floor in the X axis for excitation in the direction $X45$

4.3.4. Discretization convergence study

As mentioned in 4.3.2, the structural members of the model are discretized in order to define the loading area and apply the spectral point loads. The effect of this discretization in the resulting response of the structure is investigated with a convergence study. The vertical members (columns and diagonal braces) are ”artificially” divided into segments of ever smaller length. For every segment, the wind loads are calculated and the application of the point loads as illustrated in Figure 4.13 becomes more and more dense. Wind direction $Z45$ is chosen for this convergence study and the resulting RPSD of the top floor in the Z axis is shown in Figure 4.17, for four different segment lengths dL.

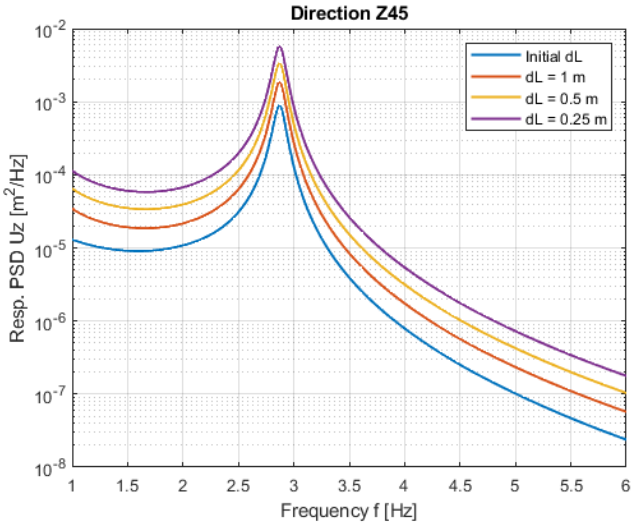

Figure 4.17: Influence of the discretization of the vertical members in the structure’s response

It is evident from the figure that the discretization of the vertical members has a significant impact in the resulting response. More specifically, the RPSD increases by decreasing the size of the segments, without converging. This disagreement between the results can be explained by the vertical distribution of the wind velocity and the influence of its logarithmic profile on the wind force (see Equation 2.11). Figure 4.18 provides a sketch of a cantilever beam for the simple case of a static wind load. For a segment that covers the whole height of the cantilever the wind force is denoted by F and if the cantilever is discretized into two segments (with half of the original area), then the resulting forces F_1 and F_2 for the case of a uniform wind profile (Figure 4.18a) are equal and half of the original force F. On the contrary, for the same segments a logarithmic profile leads to different forces F_1, F_2 highlighting the necessity of a very fine discretization, which will improve the accuracy of the results.

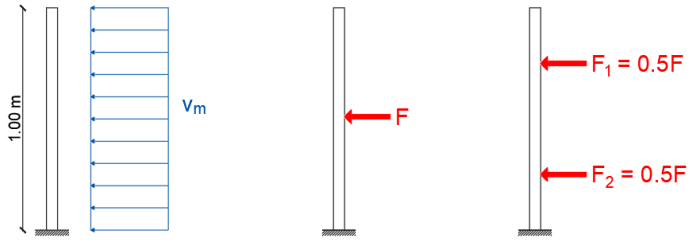

(a) Uniform wind profile and the occurring forces

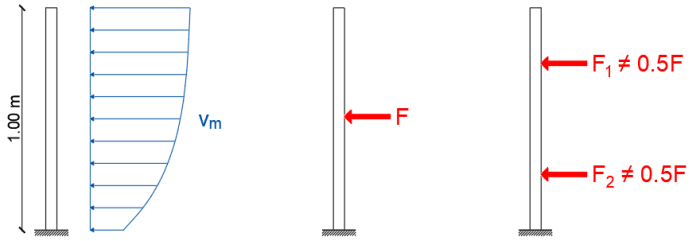

(b) Log wind profile and the occurring forces

Figure 4.18: Illustration of the influence of the wind profile on the forces of a cantilever beam

In ANSYS, the number of possible applied spectral loads in a random vibration analysis is limited, restricting thus a further investigation regarding the convergence of the response. For the remainder of this thesis, the response of the mast determined with the smallest possible segment size (0.25 m) will be used, as shown in Figure 4.17, since it is considered to be more accurate.

4.4. Conclusion

Through their shared topology, the radar experiences the vibrations of the supporting lattice structure. Therefore, it is important to evaluate those vibrations when the lattice tower is excited by a dynamic and random wind load. A finite element model is created, based on assumptions due to the limited knowledge regarding the real structure, and the natural frequencies and mode shapes of the lattice tower are found. With a random vibration analysis the structural response under the wind loading is assessed in the frequency domain. This response heavily depends on the nodal application of the spectral wind loads in the developed model. The results of the random vibration analysis will be used in the following chapter, as a loading condition for the modelling of the radar.

5

Radar model & fatigue assessment

This chapter focuses on establishing the stress response of the radar through a simplified Finite Element Model (FEM) and the subsequent evaluation of the random fatigue. Section 5.1 offers a description of the model, while in Section 5.2 the considered loading conditions are outlined and the stress response is obtained with a dynamic analysis in the time domain. Furthermore, possible failure due to fatigue is examined in Section 5.3 and an investigation of parameters that may affect the fatigue damage of the radar is discussed in Section 5.4.

5.1. Radar Finite Element Model

5.1.1. Description of the radar

The considered nautical radar system is installed on the top floor of the lattice tower that is described in the previous chapter. The system is assembled by an antenna with its turning unit and it is placed upon a pedestal that acts as the supporting structural element for the system. In Figure 5.1 the whole system is shown, as installed on the mast in Stellendam.

Figure 5.1: Nautical radar system on the mast in Stellendam

A protective case (radome) encapsulates the radar antenna, while the turning unit contains the motor that provides the required power for the rotation of the radome. Simplified drawings showing the exterior of these components are given in Figure 5.2. The left side illustrates the front view of the radar and the right one depicts the side view, while the dimensions are given in meters.

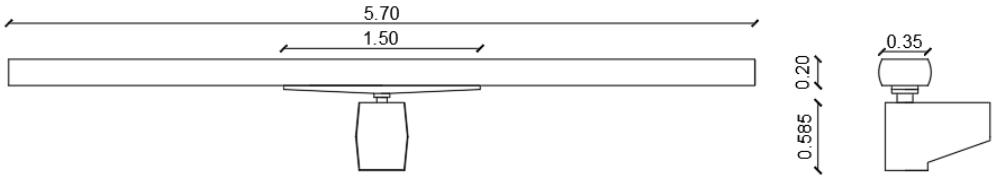

Figure 5.2: Nautical radar system on the mast in Stellendam

Between the radome and the turning unit, an extra metal member exists that supports the radome and rotates with it. This member, hereinafter called antenna arm, has a length of 1.50 m and is 0.14 m wide, while it is bolted on the bottom part of the radome (see Figure 5.3).

(a) Length of the ”antenna arm”

(b) Bolted connection

Figure 5.3: Supporting ”antenna arm” between the radome and the turning unit

5.1.2. Element type

A second, simplified FEM that represents the nautical radar system is created in ANSYS. Shell and beam elements are used as element types in the development of the model. A brief description of the beam element type was given in 4.1.2. In this case it is used for the modelling of the turning unit and the antenna arm. The shell type consists of four nodes with six DOF at each node: translations in the x,y,z directions and rotations about those axes. It is suitable for the representation of thin walled structures [44] and hence the pedestal and the radome are modelled with this type.

Special notice is given in the case of the turning unit which is shown with closer detail in Figure 5.4. This member consists of mechanical parts, such as the rotor and a gearbox, that are enclosed into a protective box. Modelling these internal items with great detail is beyond the interest of this research and thus a beam element is chosen for the representation of their rigidity and mass. An extra nodal mass is added in the beam element in order to model the mass of the rotor, which displays a small offset from the central axis of the radar system (see Figure 5.4b).

(a) Protective case of the turning unit

(b) Rotor and mechanical assembly

Figure 5.4: Turning unit and the composition of its interior

Regarding the modelling of the antenna, the Lange Jaap incident is the driving force for the choice of the element type and the subsequent assessment of the fatigue damage. The occurring failure in that case concerned the exterior part of the antenna, as shown in Figure 5.5, where the upper part of the radome was separated from its bottom side. Therefore, for the current FEM in this research, the shell element is used for modelling only the external part of the antenna, omitting any internal components. As a result, an empty and very thin (7.5 mm) member is created. In reality though, the radome encloses a linear waveguide and a protective foam material, but the weight and stiffness of those items are assumed to be negligible.

Figure 5.5: Failure of the radome in the Lange Jaap incident

5.1.3. Material properties and boundary conditions

In contrast to the development of the FEM in Chapter 4, where all structural members of the lattice tower were known to be made of steel, the materials used in the assembly of the nautical radar system are unknown with the exception of the pedestal (steel). The only information available regarding the properties of the system, is its total mass of 560 kg. For this reason, the considered materials and their assigned properties are based on assumptions, although this affects the overall accuracy of the generated model. An overview of the chosen material for each component of the radar system is presented in Table 5.1.

Table 5.1: Components of the nautical radar system and their assigned element types and materials

Radar component	Element type	Material
Pedestal	Shell	Steel
Turning unit	Beam	Steel
Antenna arm	Beam	Aluminium
Antenna radome	Shell	GFRP

The greatest uncertainty around the construction of the nautical radar system concerns the material used for the antenna radome. More importantly, the modelling choice regarding this material has a significant impact in the fatigue life prediction, because the evaluation of a possible fatigue failure focuses on this specific component, as explained in 5.1.2. In this case, Glass Fiber Reinforced Polymer (GFRP) is selected as the material used for the radome, based on a similar maritime radar [28], while its general properties are given in Table 5.2.

Table 5.2: Typical GFRP material properties [52]

Material property	Value
Density $[kg/m^3]$	2000
Young's Modulus EX $[GPa]$	35
Young's Modulus EY $[GPa]$	10
Young's Modulus EZ $[GPa]$	10
Poisson's ratio VXY [-]	0.25
Poisson's ratio VYZ [-]	0.30
Poisson's ratio VXZ [-]	0.25

Regarding the boundary conditions, a revolute joint is placed between the antenna arm and the turning unit, which allows the arm and the radome to rotate around the vertical axis while rotations around the two other axes are prohibited. Furthermore, the bottom part of the model is initially fixed, restricting all displacements and rotations at the base of the pedestal. Finally, the connections between the different element types (with varying mesh densities) are modelled based on the work by Huo et al. [22]. The resulting FEM is displayed on Figure 5.6.

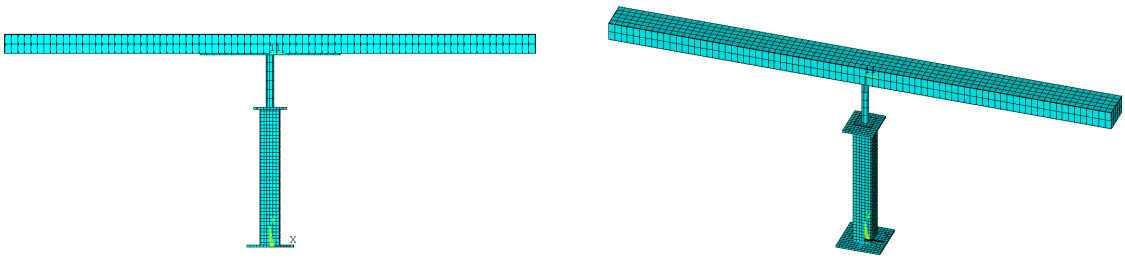

(a) Front view (b) 3D view

Figure 5.6: Nautical radar system FEM in ANSYS

5.2. Stress development at the antenna radome

5.2.1. Modelling of the loading conditions

In order to determine the development of stress at the surface of the radome, first the loading conditions of the nautical radar system have to be distinguished as follows (see also Figure 5.7):

- Wind loading while the antenna is rotating (Figure 5.7a).
- Motion of the whole radar system due to the vibrations of the lattice tower (Figure 5.7b).

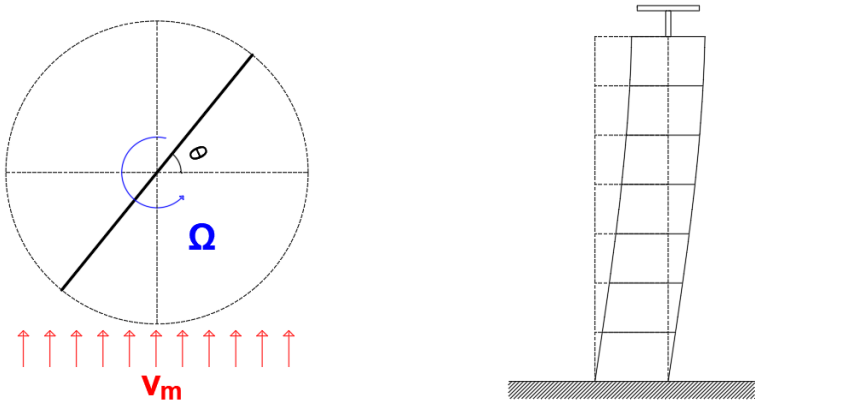

(a) Wind blowing in the rotating antenna (b) Shared motion of the radar with the mast

Figure 5.7: Simplified illustration of the acting effects on the radar

Rotation of the antenna

In reality, the motor inside the turning unit provides the necessary torque for the rotation of the antenna, while in the model an angular velocity Ω about the rotational axis is applied on the rotating components (radome & antenna arm). According to the manufacturer, the radar can rotate with a constant Ω depending on the level of the incoming wind velocity. Based on these specifications, the value of the angular velocity Ω is selected to be 20 rpm, meaning that the antenna completes one full revolution in 3 seconds.

Wind loading

For the modelling of the incoming wind, only the direction $Z45$ (see Chapter 4, Figure 4.12) is considered, while the flow retardation inside the swept area [18] [57] is neglected. Furthermore, instead of visualizing the distribution of the flow with a complete CFD analysis, the wind loads are simplified with the drag force in the along-wind direction, which is described in Chapter 2. The drag force equation is repeated in this section for clarity:

$$F_D(t) = \frac{1}{2} \cdot C_D \cdot \rho \cdot A \cdot U^2(t) \tag{5.1}$$

Contrary to the case of the lattice tower, where the wind velocity and the subsequent wind loads are modelled in the frequency domain, the time domain is selected in this occasion. The choice for the modelling domain is based upon the fact that the model of the radar system includes non-linear geometrical effects, since the antenna is rotating about the vertical axis through the revolute joint. Hence, using the Shinozuka method, which is described in detail in Chapter 2, random time-series of the incoming wind velocity can be generated from the Solari turbulence spectrum, at any node of the developed radar FEM. An example of a simulation of the wind velocity for a node in the antenna radome (22.237 m height above ground) is shown in Figure 5.8a. In order to verify the validity of the simulation method, a comparative analysis is conducted, between the theoretical wind spectrum (Solaris) and the computed spectrum obtained by spectral analysis of the simulated sample time-history. The results are depicted in logarithmic scale in Figure 5.8b, where a very good agreement between the two spectra is observed.

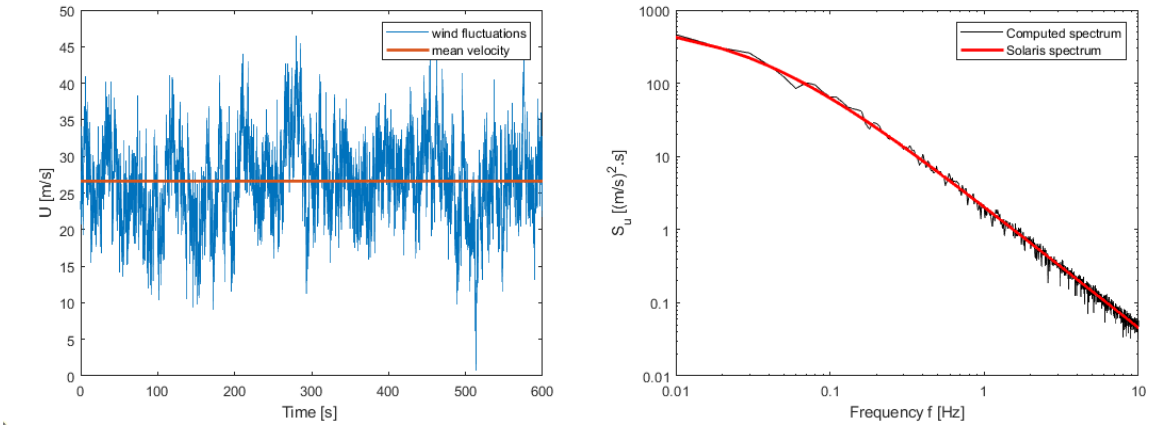

(a) Generated wind velocity time-history

(b) Comparison between theoretical and computed spectrum

Figure 5.8: Simulating result of wind velocity at the mid-point of the radome

With the generated wind velocity time-history, the corresponding wind force applied on the radar system is calculated with Equation 5.1. For the nodal application of the wind load, the geometry of the system is once again discretized into segments and thus the drag force is applied as a point load for each segment. However, the loading area of each segment of the radome does not remain constant since the antenna is rotating. For this reason, the drag force is multiplied with the absolute value of a cosine modulating function $\cos(\Omega t)$, where Ω is the angular velocity of the antenna. The absolute value is taken in order to keep a constant sign (direction) of the force. The effect of this function on the wind load is illustrated on Figure 5.9a, for a node of the radome. The load in this graph is calculated for a radome with an imaginary zero width, for the purpose of making visible the effect of the modulating function. The depicted duration concerns the first two revolutions of the antenna and it is assumed that at $t = 0$, the wind is blowing perpendicularly to the radome. The two signals overlap when the antenna is located in a position perpendicular to the wind and the loading area approaches its full value, whereas for the rest of the time the force is overestimated without the modulating function. In the actual model the radome has a non-zero width and thus, the surface facing the wind changes due to the rotation of the radome. Figure 5.9b depicts the wind load interchanging between the surfaces in the length dimension of the radome.

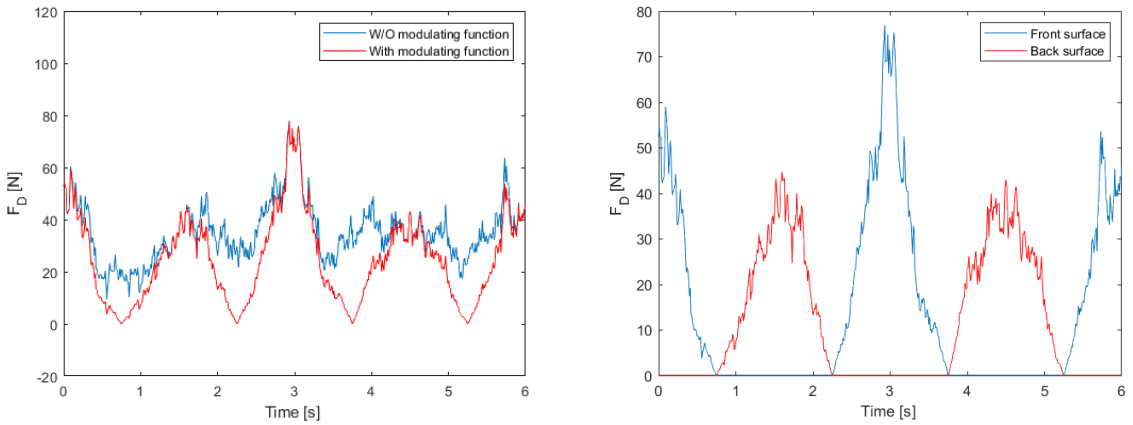

(a) Effect of the modulating function on the wind load

(b) Loaded surfaces in the length dimension of the radome

Figure 5.9: Wind load at the antenna radome

Base motion of the radar system

The radar shares the same vibrations with the tower below due to their common topology. Therefore, the results from the random vibration analysis in Chapter 4 are used as input for the considered loading condition. The response spectral densities of the displacements in the top floor of the tower are shown in Figure 5.10 for the wind direction $Z45$. As can be seen from the figure, the structural response in the Z axis (UZ) is larger than the corresponding ones in the other two directions. It is therefore assumed that as a starting point, the motion of the radar consists only of the displacement UZ and thus the DOF for the translation in the Z axis at the bottom part of the radar's FEM are released, while the rest remain restricted.

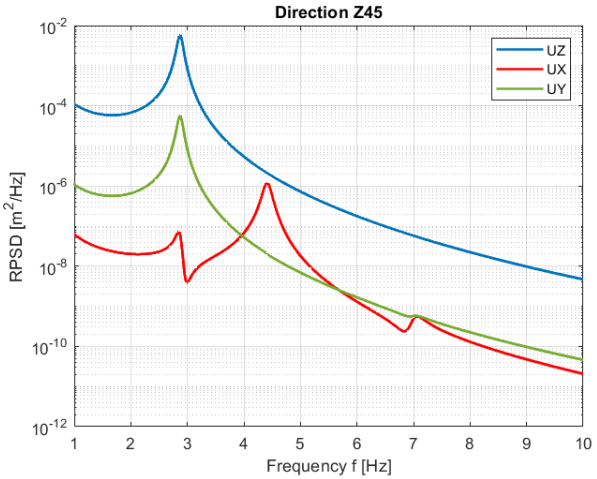

Figure 5.10: Response spectra of the top floor's displacements in all axes for excitation in the direction $Z45$

Due to the fact that the random vibration analysis of the previous chapter occurs in a linear system, the response of the lattice tower is considered to be a stationary Gaussian process like the input of the system (wind loading) [59]. As a result, time-series of the response can be generated similarly to the wind velocity simulations. A sample of the resulting displacement in the Z axis is given in Figure 5.11.

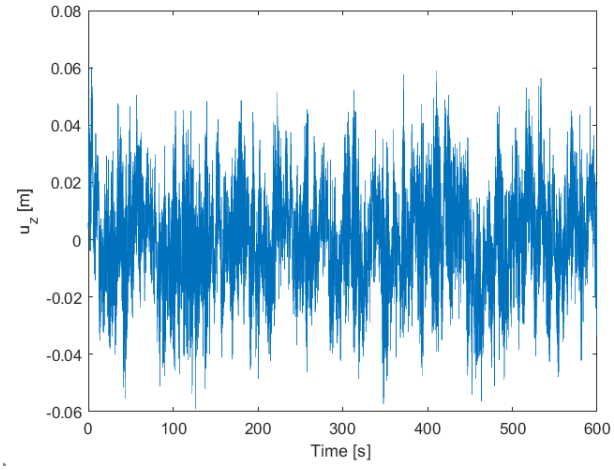

Figure 5.11: Generated displacement time-history in the Z direction

5.2.2. Results

A summary of the aforementioned loading conditions is illustrated in Figure 5.12. These actions are considered to occur simultaneously and a time-history analysis is performed in ANSYS, in order to determine the dynamic response of the nautical radar system. Due to the computational cost, the duration of the time-history is chosen as 12 seconds (four revolutions of the antenna).

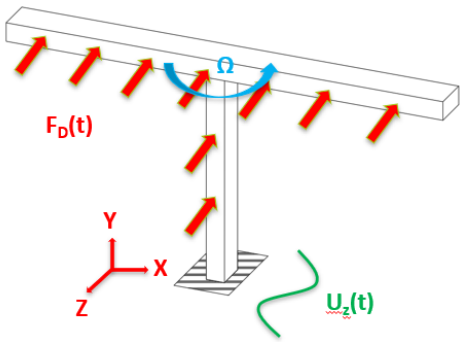

Figure 5.12: Sketch representation of the loads acting on the radar

Based on the Lange Jaap incident, the development of stresses at the bottom part of the radome is the subject of investigation for the performed analysis. Figure 5.13 depicts the resulting σ_x stresses at two different snapshots in time, where it is evident that the critical area for the development of stresses is the shared area between the antenna arm and the bottom part of the radome. In fact, during the duration of the time-history analysis, the magnitude of the σ_x stress in this area varies from 2 to almost 60 times higher than the rest of the bottom surface.

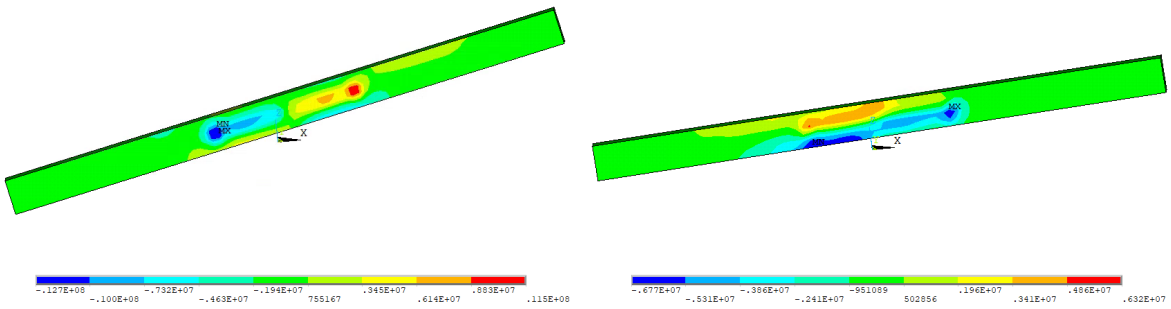

Figure 5.13: Stress (σ_x) development at the bottom part of the radome

The resulting stress time-history for an element of the radome in the neighbouring area with the antenna arm is plotted in Figure 5.14a. The first revolution of the antenna is omitted from the time-history, for the purpose of excluding the effect of the initial conditions. In an effort to distinguish which loading condition is more influential in the stress response, the dynamic analysis in ANSYS is run separating the base motion from the wind load. As clearly seen in Figure 5.14b, for one specific sample of wind velocity and displacement, the stress generated from the wind load is negligible compared to the corresponding one from the base motion of the radar, which is almost 15 times higher in terms of stress amplitude. Hence, it can be stated that the base motion is considered predominant for the response of the specific radar model that is developed in this thesis.

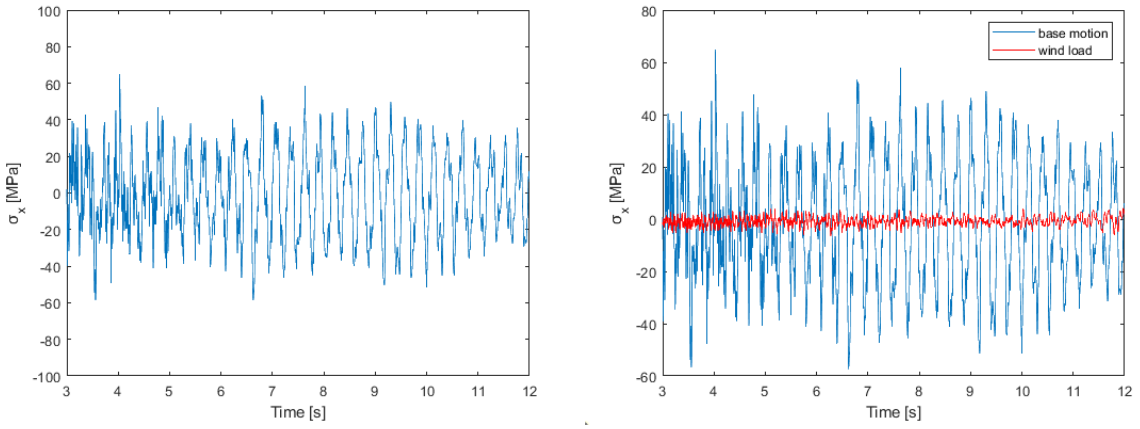

(a) σ_x when the loading conditions act simultaneously (b) σ_x when the loading conditions are considered individually

Figure 5.14: Stress time-histories for an element at the bottom part of the radome

5.3. Fatigue assessment

Since the wind velocity and the motion of the radar are treated as stochastic processes, their generated time-series, which are used as the input to the performed dynamic analysis, describe only possible realizations of the loading conditions. Therefore, the depicted stress time-history in Figure 5.14 does not express a deterministic outcome of the analysis but instead the stress should also be considered as a random process. For the fatigue life prediction of the radar a probabilistic approach is hence needed, as explained in Chapter 3.

Due to the fact that the dynamic analysis is non-linear and because a high accuracy is desired, the time domain is chosen in this occasion for the evaluation of the fatigue. Taking into account the computational cost, 25 simulations (with different seeds) are considered and the analysis is run in ANSYS for each simulation. The building blocks of Chapter 3 (see Figure 3.5) are applied in order to assess the fatigue damage for each simulation and the final fatigue damage is taken as the mean of the 25 separately calculated values. The stress ranges and their corresponding number of occurrences obtained with the rainflow algorithm, are shown in Figure 5.15 for the stress time-history of Figure 5.14a.

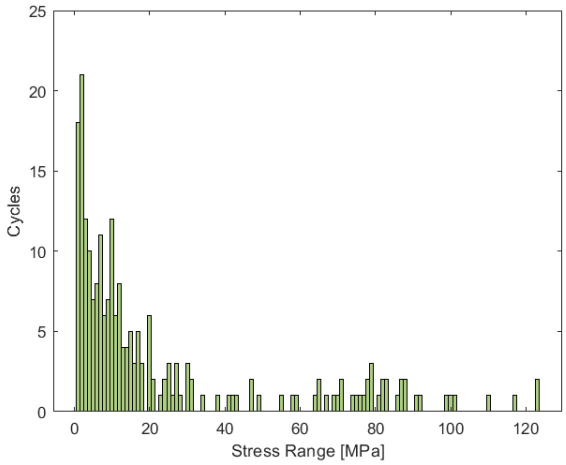

Figure 5.15: Distribution of stress ranges

Nevertheless, the time-history analysis in ANSYS concerns only the first revolutions of the antenna, assuming that before $t = 0$ the radar was standing still. In order to calculate the fatigue damage for a period of 1 year, the duration of the time-history needs to be extended, which is deemed impractical due to the computational cost. However, the stress signal in Figure 5.14a follows a similar pattern and does not depict any obvious trend. The assumption is then made, that the signal remains stationary and repeats over the period of 1 year. This implies though, that the loading conditions remain unchanged during 1 year (i.e. the wind blows with the same wind velocity), which significantly impacts the accuracy of the results.

As mentioned in 5.1.3, the radome is assumed to be constructed with a GFRP material. However, for the selection of the S-N curve and the construction of the Goodman diagram a further assumption is necessary regarding the strength properties of the material. Because of the extensive usage of GFRP composites in the fabrication of wind turbine blades, the tensile strength UTS and the compressive strength UCS are taken as 428 MPa and 291 MPa respectively, based on GFRP speciments used by Van Delft et al. [54]. With those values, the permissible number of cycles are obtained from the Goodman diagram (see Section 3.3 of Chapter 2) and using the Palmgren-Miner rule, the 1-year fatigue damage is calculated for each of the 25 simulations. The resulting averaged 1-year fatigue damage and the corresponding lifetime is presented in Table 5.3:

Table 5.3: 1-year fatigue damage and lifetime prediction

$D_{1,avg}$ [-]	T_f [years]
56.9	0.017

5.4. Sensitivity study

The previously described fatigue evaluation is based upon a series of assumptions used throughout this research. For this reason, a sensitivity analysis is carried out in order to investigate the impact of specific modelling choices or parameters in the fatigue lifetime prediction. The parameters chosen for this sensitivity study are listed below and their influence is elaborated in the upcoming sections:

- Strength properties of the antenna radome's material
- UX, UY displacements at the base of the radar
- UZ displacement at the base of the radar
- Material of the antenna arm

5.4.1. Influence of the radome's strength properties

In Section 5.3, the values for the strength properties (UTS, UCS) of the antenna radome were assumed as 428 MPa and 291 MPa respectively, leading to an almost immediate fatigue failure. These values are now increased and taken as 690 MPa (UTS) and 580 MPa (UCS) according to [3], in order to determine the impact of the material's durability in the fatigue damage. The results are given in Table 5.4, where it is evident that the material strength properties significantly affect the fatigue lifetime prediction, which is increased from a practically zero value to nearly 19 years.

Table 5.4: Comparison between the fatigue results obtained with the initial strength properties versus increased ones

	Initial UTS,UCS	Increased UTS,UCS	Rel. change [%]
$D_{1,avg}[-]$	56.9	0.053	-99.90
$T_f[years]$	0.017	18.7	+109900

5.4.2. Influence of the UX, UY base displacements

In Section 5.2.1, the motion of the radar due to the vibrations of the tower below was assumed to be consisted only of the displacement UZ. However, this motion turned out to be the dominant loading condition for the development of stresses at the bottom part of the radome. Thus, the question arises whether the displacements of the tower's top floor in the other two axes (UX, UY), would influence the evaluation of the fatigue.

From the previously depicted response spectral densities (see Figure 5.10), time-history simulations are generated for the displacements in the X and Y directions, which are plotted in Figure 5.16. The dynamic analysis in ANSYS is now run using the combined base motion in the three directions and also the wind loading, for 25 realizations. Finally, using the material strength properties assumed in 5.4.1, the resulting 1-year fatigue damage and the fatigue lifetime are shown in Table 5.5, where a 38 % relative decrease in the lifetime is noticed, compared to the results of 5.4.1.

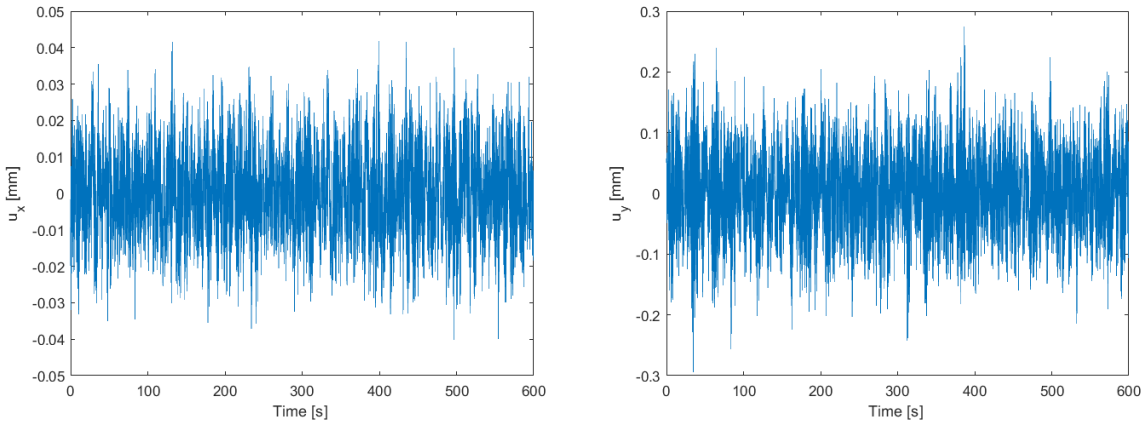

(a) Displacement time-history in the X direction

(b) Displacement time-history in the Y direction

Figure 5.16: Generated simulations for the base motion

Table 5.5: Comparison between the fatigue results obtained with only the UZ displacement versus the three translational motions

	Only UZ	UZ,UX,UY	Rel. change [%]
$D_{1,avg}[-]$	0.053	0.086	+62.26
$T_f[years]$	18.7	11.54	-38.28

5.4.3. Influence of a larger UZ displacement

At the end of Chapter 4 (see 4.3.4), it was concluded that the discretization of the lattice structure for the nodal application of the spectral wind loads has a significant impact in the response of the tower's top floor. Due to the limitation of ANSYS regarding the number of applied spectral loads, the final obtained response of the lattice tower is underestimated. For this reason, the spectral values of the UZ response, which were obtained for the lattice tower with a random vibration analysis in Chapter 4, are multiplied by a factor of 1.50 and a new, increased UZ displacement is generated in the time domain. The dynamic analysis in ANSYS is run once again for 25 realizations of the displacement UZ and the wind turbulence (the turbulence simulations are the same as in the previous sections). Using the UTS, UCS values of 5.4.1, the averaged 1-year fatigue damage is obtained. The results are shown in Table 5.6, where an extreme reduction in the fatigue lifetime is observed, as it is decreased to nearly 0 years compared with the lifetime of 18.7 years, which was found with the initial displacement UZ.

Table 5.6: Comparison of the fatigue results obtained with the initial UZ displacement versus an increased one

	Initial UZ	Increased UZ	Rel. change [%]
$D_{1,avg}[-]$	0.053	33.14	+62428
$T_f[years]$	18.7	0.03	-99.83

5.4.4. Influence of the antenna arm's material

All the previously mentioned fatigue results were obtained for the assumed materials of the nautical radar system that are described in Table 5.1. In this section, the construction material of the antenna arm is changed from aluminium to steel, whereas the rest of the materials remain the same. The fatigue evaluation is performed using the same 25 realizations of the UZ displacement and the wind turbulence as in Section 5.3, with the material strength properties of 5.4.1. Table 5.7 compares the results obtained for the case of a steel antenna arm, with the previous results, where an aluminium material was assumed. Using a steel antenna arm leads to a nearly 29 times higher fatigue lifetime and thus, it can be stated that the modelling choice for the material of the antenna arm heavily influences the resulting fatigue of the radome. The difference between the two scenarios might be explained by the influence of the material properties in the dynamic properties of the radar system. An antenna arm made of steel would result in an increase of the natural frequencies, which appears to affect positively the response of the radar system, when excited by the wind load and the motion at the base.

Table 5.7: Comparison of the fatigue results obtained for an antenna arm made of aluminium versus a steel one

	Aluminium arm	Steel arm	Rel. change [%]
$D_{1,avg}[-]$	0.053	0.00187	-96.47
T_f [years]	18.7	534	+2755

5.5. Conclusion

In operational mode, the rotating antenna of the radar experiences the influence of the wind, while it shares the vibrations of its supporting structure. In order to evaluate the impact of these loading conditions, a separate finite element model is developed and a dynamic analysis is performed in the time domain due to the non-linear geometry of the considered model. The central area of the radome's bottom surface is identified to be the critical part with respect to the stress development, whereas the effect of the wind in the response of the developed radar model appears to be very small. A probabilistic approach is followed for the assessment of the fatigue, due to the random nature of the loading conditions, and the results show that both the material properties of the radar system and the translational motions at the base of the radar play a major role in the fatigue lifetime prediction.

6

Conclusions & recommendations

In the following paragraphs, conclusions are drawn according to the identified research objective and the formulated questions given in Chapter 1, whereas a critical review of the research and recommendations for future studies are also discussed.

6.1. Conclusions

Before introducing the conclusions drawn from the current thesis, it is important to note that a number of assumptions have been established during the suggested approach. The main findings of this research are thus, heavily relied upon specific modelling choices and decisions. The most influential assumptions are summarized below:

- The lattice tower and the radar system are treated separately.
- In the tower's FEM, the radar system is modelled as an added mass.
- The wind load on the rotating antenna is modelled only in the along-wind direction.
- A GFRP composite is selected as the material used for the antenna radome.

Taking into consideration the above assumptions, the answers to the main research questions of Chapter 1 can now be formulated:

1. Which part of the radar is critical for the fatigue investigation?

   In this study, a potential fatigue failure is focused on the external, protective case (radome) of the radar antenna and more specifically at its bottom surface. The presence of a horizontal, supporting metal component (antenna arm), attached to the bottom part of the radome, considerably affects the development of stresses. The shared area between this metal component and the bottom surface of the radome is identified as the critical part of the radome, where the magnitude of the developed stress is significantly larger than the rest of the surface.

2. Which loading condition is governing for the response of the radar?

   For the developed model of the radar system, the effect of the wind at the antenna radome is found to be very small compared to the corresponding effect due to the motion at the base of the radar, meaning that the vibrations induced through the lattice tower appear to be the governing loading condition. However, this result is strongly dependent upon the fact that the complete fluid-structure interaction in the 3D space is not

considered, since the aerodynamic effect is approximated by only the force in the flow direction.

3. How sensitive is the fatigue damage with respect to specific parameters?

   Given the assumption of using a GFRP composite as the material for the antenna radome, the strength properties (UTS, UCS) of this material appear to extremely affect the resulting fatigue lifetime prediction. Furthermore, the magnitude of the displacement in the Z direction at the base of the radar strongly impacts the fatigue damage of the radome. Although, the initial assumption of accounting only for this displacement at the base is not justified, since it overestimates the fatigue lifetime compared to the case, where the displacements in the other two directions are considered as well. Finally, using a steel antenna arm, instead of an aluminium one, will influence positively the development of stresses at the bottom surface of the radome and the subsequent fatigue damage.

4. Will it be possible to uncouple the radar from the mast?

   In the suggested approach, the lattice tower and the radar system are treated as two separate entities and therefore, the obtained results reflect to a decoupled system. The radar is represented by a mass at the tower's top, which implies that the radar is considered as a rigid object. However, this condition might not be valid, especially since the antenna is a relatively long and slender component. An integrated, coupled FEM would display different dynamic properties and it would capture properly the interaction between the tower and the radar. More importantly though, accounting for the possible flexible behaviour of the radar in the integrated model, may have consequences in the effect of the wind at the antenna. If the local mode shape of the radar would occur in a natural frequency below the corresponding one of the first bending mode of the global system, then the low frequency content of the wind would amplify the response of the radar. In this occasion, the statement regarding the governing loading condition (see above) might also not be true. Further investigation is hence needed, in order to compare and determine the validity of the obtained results, through the suggested decoupled approach, with an integrated model.

6.2. Recommendations

In conclusion, the proposed approach and the developed models can be used as the foundation for the assessment of the structural health of nautical radar systems. However, further research is necessary, aiming to verify and improve the accuracy of the suggested models of this thesis. To this end, and besides the aforementioned suggestion regarding an integrated (coupled) model, the following recommendations for future investigation are identified:

- It is deemed necessary to verify the developed models with measurements. In fact, a parallel thesis in TU Delft is ongoing, with the scope of identifying the vibrations of the radar by placing acceleration sensors at the nautical radar system in Rijkswaterstaat's Offshore Expertise Center. Cross-validating the results and updating the model with real data can be very valuable for future applications.
- Due to the lack of information regarding the construction details and the material properties of the radar system, the developed radar model is characterized by a high degree of uncertainty. Therefore, taking into account those existing uncertainties will turn out to be an important improvement of the model.

- The scenario of having a different supporting structure for the nautical radar system can be investigated. More specifically, since Rijskwaterstaat is currently installing these sensors on offshore wind farms, an extremely interesting and important scenario would be the case of a wind turbine as the supplementary structure for the radar. The motion of the wind turbine may have detrimental results for the structural integrity of the radar, while extra caution should be given also, in the impact of the passing turbine blades during operation.

Bibliography

[1] Barltrop, N. D. P. and Adams, A. J. (1991). *Dynamics of fixed marine structures*. Butterworth-Heinemann, 3rd edition.

[2] Bojórquez, E., Payán-Serrano, O., Reyes-Salazar, A., and Pozos, A. (2016). Comparison of spectral density models to simulate wind records. *KSCE Journal of Civil Engineering 2017 21:4*, 21(4):1299–1306.

[3] Burton, T., Jenkins, N., Sharpe, D., and Bossanyi, E. (2011). *Wind energy handbook*. John Wiley & Sons.

[4] Chopra, A. K. (2017). *Dynamics of Structures: Theory and Applications to Earthquake Engineering*. Pearson, 5th edition.

[5] Cook, R. D., Malkus, D. S., Plesha, M. E., and Witt, R. J. W. (2002). *Concept and Applications of Finite Element Analysis*. John Wiley & Sons, 4th edition.

[6] Davenport, A. G. (1967a). Gust Loading Factors. *Journal of the Structural Division*, 93(3):11–34.

[7] Davenport, A. G. (1967b). The dependence of wind loads on meteorological parameters.

[8] de Klerk, D., Rixen, D. J., and Voormeeren, S. N. (2008). General Framework for Dynamic Substructuring: History, Review and Classification of Techniques. *AIAA Journal*, 46(5):1169–1181.

[9] Downing, S. D. and Socie, D. F. (1982). Simple rainflow counting algorithms. *International Journal of Fatigue*, 4(1):31–40.

[10] Dyrbye, C. and Hansen, S. O. (1997). *Wind loads on structures.* Wiley, Chichester.

[11] Eurocode (2005). EN 1991-1-4, Eurocode 1: Actions on structures - Part 1-4: General actions - Wind actions.

[12] Eurocode (2006). EN 1993-3-1, Eurocode 3: Design of steel structures - Part 3-1: Towers, masts and chimneys - Towers and masts.

[13] Eurocode (2020). National Annex to EN 1991-1-4, Eurocode 1: Actions on structures - Part 1-4: General actions - Wind actions.

[14] Gathercole, N., Reiter, H., Adam, T., and Harris, B. (1994). Life prediction for fatigue of T800/5245 carbon-fibre composites: I. Constant-amplitude loading. *International Journal of Fatigue*, 16(8):523–532.

[15] Germanischer Lloyd Industrial Services GmbH (2010). Guideline for the Certification of Offshore Wind Turbines.

[16] Haiford, G. R. (1997). Cumulative fatigue damage modeling—crack nucleation and early growth. *International Journal of Fatigue*, 19(93):253–260.

[17] Holmes, J. D. (2002). Fatigue life under along-wind loading — closed-form solutions. *Engineering Structures*, 24(1):109–114.

[18] Homicz, G. F. (1991). Numerical simulation of VAWT stochastic aerodynamic loads produced by atmospheric turbauence: VAWT-SAL code. Technical report.

[19] Horn, J.-T. and Jensen, J. (2016). Reducing Uncertainty of Monte Carlo Estimated Fatigue Damage in Offshore Wind Turbines Using FORM. *International Journal of Electrical, Computer, Energetic, Electronic and Communication Engineering*, 10:988–997.

[20] Huo, T. and Tong, L. (2020a). An approach to wind-induced fatigue analysis of wind turbine tubular towers. *Journal of Constructional Steel Research*, 166:105917.

[21] Huo, T. and Tong, L. (2020b). Wind-induced response analysis of wind turbine tubular towers with consideration of rotating effect of blades. *Advances in Structural Engineering*, 23(2):289–306.

[22] Huo, T., Tong, L., and Zhang, Y. (2018). Dynamic response analysis of wind turbine tubular towers under long-period ground motions with the consideration of soil-structure interaction. *Advanced Steel Construction*, 14(2):227–250.

[23] Huo, T., Tong, L. W., and Mashiri, F. R. (2019). Turbulent wind field simulation of wind turbine structures with consideration of the effect of rotating blades. *Advanced Steel Construction*, 15(1):82–92.

[24] Jia, J. (2014). Investigations of a practical wind-induced fatigue calculation based on nonlinear time domain dynamic analysis and a full wind-directional scatter diagram. *Ships and Offshore Structures*, 9.

[25] Joosse, P. A., Van Delft, D. R., Rink, H. D., and Bach, P. W. (1994). Fatigue behaviour of fibreglass wind turbine blade material at the very high cycle range.

[26] Kawai, M. and Koizumi, M. (2007). Nonlinear constant fatigue life diagrams for carbon/epoxy laminates at room temperature. *Composites Part A: Applied Science and Manufacturing*, 38(11):2342–2353.

[27] Ke, S. T., Ge, Y. J., Wang, T. G., Cao, J. F., and Tamura, Y. (2015). Wind field simulation and wind-induced responses of large wind turbine tower-blade coupled structure. *Structural Design of Tall and Special Buildings*, 24(8):571–590.

[28] Lestari, A. A., Hakkaart, P., Zijderveld, J. H., Zwan, F. V., Hajian, M., and Ligthart, L. P. (2008). INDRA: The indonesian maritime radar. In *Proceedings of the 38th European Microwave Conference, EuMC 2008*, pages 1600–1603.

[29] Lin, Y.-K. (1967). *Probabilistic theory of structural dynamics*. McGraw-Hill.

[30] Liu, Y. and Mahadevan, S. (2020). Probabilistic fatigue life prediction of composite materials. *Fatigue Life Prediction of Composites and Composite Structures*, pages 607–633.

[31] Lombardi, G. (1989). Wind-tunnel tests on a model antenna with different fin configurations. *Engineering Structures*, 11(3):134–138.

[32] Lombardi, G. (1991). Wind-tunnel tests on a model antenna rotating in a cross flow. *Engineering Structures*, 13(4):345–350.

[33] Luigi Ascione, Wouter De Corte, Patrice Godonou, Jean Knippers, Eric Moussiaux, Toby Mottram, Matthias Oppe, Nuno Silvestre, Peter Thorning, Liesbeth Tromp, and S Maria Paganica Church (2017). Prospect for New Guidance in the Design of FRP Structures.

[34] Madugula, M. K. (2001). *Dynamic response of lattice towers and guyed masts*. ASCE Publications.

[35] Mandell, J. F., Samborsky, D. D., Wang, L., and Wahl, N. K. (2003). New Fatigue Data for Wind Turbine Blade Materials. *Journal of Solar Energy Engineering*, 125(4):506–514.

[36] Manwell, J., McGowan, J., and Rogers, A. (2010). *Wind energy explained: theory, design and application*.

[37] Miner, M. (1945). Cumulative damage in fatigue. *journal of applied mechanics 12 no. 3*, pages A159–A164.

[38] Muggiasca, S., Ripamonti, F., Rocchi, D., and Zasso, A. (2009). Numerical And Experimental Investigation On A Maritime Radar Scanner. *WIT Transactions on The Built Environment*, 105:313–322.

[39] Nijssen, R. P. (2020). Phenomenological fatigue analysis and life modeling. *Fatigue Life Prediction of Composites and Composite Structures*, pages 47–75.

[40] Nijssen, R. P. L. (2006). Fatigue life prediction and strength degradation of wind turbine rotor blade composites.

[41] Palmgren, A. (1924). Die lebensdauer von kugellargern. *Zeitshrift des Vereines Duetsher Ingenieure*, 68(4):339.

[42] Philippidis, T. P. and Vassilopoulos, A. P. (1999). Fatigue Strength Prediction under Multiaxial Stress. *Journal of Composite Materials*, 33(17):1578–1599.

[43] Philippidis, T. P. and Vassilopoulos, A. P. (2002). Complex stress state effect on fatigue life of GRP laminates.: part I, experimental. *International Journal of Fatigue*, 24(8):813–823.

[44] Rao, S. S. (2010). *The Finite Element Method in Engineering*. Elsevier, 5th edition.

[45] Shinozuka, M. (1972). Monte Carlo solution of structural dynamics. *Computers & Structures*, 2(5-6):855–874.

[46] Shinozuka, M. (1987). Stochastic Fields and their Digital Simulation. *Springer*, pages 93–133.

[47] Slavič, J., Boltezar, M., Mrsnik, M., Cesnik, M., and Javh, J. (2020). *Vibration Fatigue by Spectral Methods: From Structural Dynamics to Fatigue Damage–Theory and Experiments*. Elsevier.

[48] Solari, G. (1993). Gust buffeting. I: Peak wind velocity and equivalent pressure. *Journal of Structural Engineering*, 119:365–382.

[49] Stathopoulos, T. and Baniotopoulos, C. (2007). *Wind effects on buildings and design of wind-sensitive structures*, volume 493. Springer Science & Business Media.

[50] Strømmen, E. (2010). *Theory of bridge aerodynamics*.

[51] Tamura, Y. and Kareem, A. (2013). *Advanced Structural Wind Engineering*.

[52] Tauqeer, M. and Ong, M. (2017). Assessment of Impact Damage Caused by Dropped Objects on Glass Reinforced Plastic (GRP) Covers. In *Proceedings of the ASME 2017 36th International Conference on Ocean, Offshore and Arctic Engineering*.

[53] Thomsen, K. (1998). The statistical variation of wind turbine fatigue loads. Technical report, Riso National Laboratory, Roskilde, Denmark.

[54] Van Delft, D. R., De Winkel, G. D., and Joosse, P. A. (1997). Fatigue behaviour of fibreglass wind turbine blade material under variable amplitude loading. *35th Aerospace Sciences Meeting and Exhibit*.

[55] Van der Hoven, I. (1957). Power spectrum of horizontal wind speed in the frequency range from 0.0007 to 900 cycles per hour. *Journal of Atmospheric Sciences*, 14(2):160–164.

[56] Vassilopoulos, A. P. and Nijssen, R. P. (2020). Fatigue life prediction under realistic loading conditions. *Fatigue Life Prediction of Composites and Composite Structures*, pages 387–423.

[57] Veers, P. (1984). Modeling stochastic wind loads on vertical axis wind turbines. In *SAND83-1909*, volume 19.

[58] Vickery, B. J. (1965). On the flow behind a coarse grid and its use a model of atmospheric turbulence in studies related to wind loads on buildings. *NPL Aero Report 1143*.

[59] Vrouwenvelder, A. (2004). Lecture notes random vibrations.

[60] Wahba, Y. M., Madugula, M. K., and Monforton, G. R. (1998). Evaluation of non-linear analysis of guyed antenna towers. *Computers & Structures*, 68(1-3):207–212.

A

Random variables and random processes

In the field of engineering there are many phenomena which are nondeterministic. Any quantity, that cannot be predicted precisely is known as a random variable. However, statistical properties of the phenomenon can be deduced either by mathematical models or by recording the phenomenon multiple times during a sufficient period. Therefore, the phenomenon is described as a random process and any measured sample during a time period is called a realization of the process.

A.1. Probability distribution, mean value and variance

For a continuous random variable X, its probability density function $p(x)$ is defined as:

$$Pr[x \leq X \leq x + dx] = P(x + dx) - P(x) = \frac{dP(x)}{dx} dx = p(x)dx \tag{A.1}$$

where $P(x)$ is the probability distribution function or cumulative probability function. Since $p(x)$ is the derivative of $P(x)$, it follows that:

$$Pr[X \leq x] = P(x) = \int_{-\infty}^{x} p(x)dx \tag{A.2}$$

and when $x \to \infty$ the probability becomes 1, meaning that the area under the curve of $p(x)$ is equal to unity.

The expected value or the mean value of X is given by:

$$\mu_X = E[X] = \overline{x} = \int_{-\infty}^{+\infty} xp(x)dx \tag{A.3}$$

and the variance of X is defined as:

$$\sigma_X^2 = E[(X - \mu_X)^2] = \int_{-\infty}^{+\infty} (x - \mu_X)^2 p(x)dx \tag{A.4}$$

The square root of the variance, σ_X, is called the standard deviation of the random variable X.

When two random variables X, Y are considered, it is useful to seek their joint properties. The cross-covariance of X and Y is defined by:

$$cov_{XY} = E[(X - \mu_X)(Y - \mu_Y)] = \int_{-\infty}^{+\infty} \int_{-\infty}^{+\infty} (x - \mu_X)(y - \mu_Y) p(x, y) dx dy \tag{A.5}$$

where $p(x, y)$ is the joint probability density function of X,Y.

In wind engineering, the most important and commonly used distributions are the Gaussian and Weibull distributions. The probability density function of the Gaussian distribution is given as:

$$p(x) = \frac{1}{\sqrt{2\pi}\sigma_X} exp\left[-\frac{1}{2}\left(\frac{x - \mu_X}{\sigma_X}\right)^2\right] \tag{A.6}$$

while the Weibull probability density function is expressed as:

$$p(x) = \frac{\alpha x^{\alpha-1}}{\beta^\alpha} exp\left[-\left(\frac{x}{\beta}\right)^\alpha\right] \tag{A.7}$$

where α and β are particular shape and scale parameters, respectively. In some occasions the Rayleigh distribution is also used, which is the Weibull distribution with $\alpha = 2$.

A.2. Random processes

Auto-correlation of a random process

If $X(t)$ describes a random process then there are multiple random variables X_1, X_2 ... at different times t_i $(i = 1, 2, \ldots)$ of the process. The statistical connection between the values of $X(t)$ at different times is described by the auto-correlation function as:

$$R_X(t_1, t_2) = E[X_1 X_2] = \int_{-\infty}^{+\infty} \int_{-\infty}^{+\infty} x_1 x_2 p(x_1, x_2) dx_1 dx_2 \tag{A.8}$$

Stationary random process

A random process $X(t)$ is called stationary when its probability density function does not change over time, meaning that its statistical properties such as the mean or variance are time-independent and that the auto-correlation function depends only on the time difference $\tau = t_2 - t_1$:

$$R_X(\tau) = E[X(t)X(t + \tau)] \tag{A.9}$$

Power spectral density

The power spectral density describes how the variance is distributed over the frequency content of a random process. For the case of a stationary process, the power spectral density function is defined as the Fourier transform of the auto-correlation function (Wiener-Khintchine relation):

$$S_X(\omega) = \frac{1}{2\pi} \int_{-\infty}^{+\infty} R_X(\tau) e^{-i\omega\tau} d\tau \tag{A.10}$$

which gives:

$$R_X(\tau) = \int_{-\infty}^{+\infty} S_X(\omega) e^{i\omega\tau} d\omega \tag{A.11}$$

Assuming a zero mean value, the variance of $X(t)$ is then given by:

$$\sigma_X^2 = \int_{-\infty}^{+\infty} S_X(\omega) d\omega \tag{A.12}$$

B

Wind parameters

In Chapter 2, the determination of the mean wind velocity and the turbulence spectrum is described according to Eurocode [11], where the main wind parameters required are the following:

- fundamental basic wind velocity, v_b
- roughness length, z_0
- minimum height below which the velocity is kept constant, z_{min}

The fundamental basic wind velocity v_b is prescribed by the Dutch National Annex to Eurocode [13], based on a classification of the Netherlands into three wind areas (see Figure B.1). The values of v_b are given in Table B.1, for each one of the wind areas.

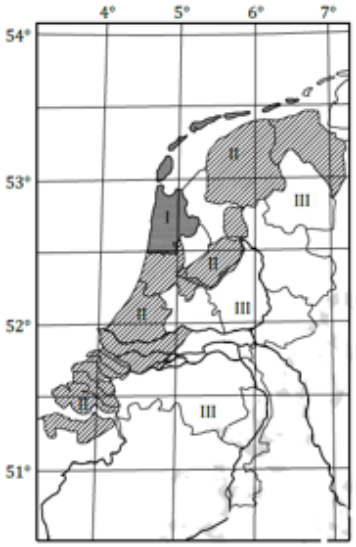

Figure B.1: Division of the Netherlands into wind areas [13]

Table B.1: Fundamental basic wind velocity for use in the Netherlands [13]

Wind area	**I**	**II**	**III**
$\mathbf{v_b}$ [m/s]	29.5	27	24.5

In addition, the roughness length z_0 and the minimum height z_{min} are defined according to Table B.2, depending on the terrain category. For the specific case of the Netherlands, the

National Annex provides three terrain categories and the corresponding parameters are presented in Table B.3.

Table B.2: Terrain categories and terrain parameters [11]

Terrain category	z_0 [m]	z_{min} [m]
0 Sea or coastal area exposed to the open sea	0.003	1
I Lakes or flat and horizontal area with negligible vegetation and without obstacles	0.01	1
II Area with low vegetation such as grass and isolated obstacles (trees, buildings) with separations of at least 20 obstacle heights	0.05	2
III Area with regular cover of vegetation or buildings or with isolated obstacles with separations of maximum 20 obstacle heights (such as villages, suburban terrain, permanent forest)	0.3	5
IV Area in which at least 15 % of the surface is covered with buildings and their average height exceeds 15 m	1.0	10

Table B.3: Terrain parameters according to the Dutch National Annex [13]

Terrain category	z_0 [m]	z_{min} [m]
0 Sea or costal area exposed to the open sea	0.005	1
I Undeveloped area	0.2	4
II Built-up area	0.5	7

C

Response of a SDOF system under random excitation

Figure C.1 shows a typical SDOF system comprised of mass m, spring with stiffness k and viscous damping c, excited by a stationary Gaussian process.

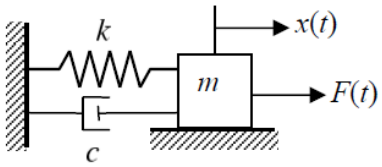

Figure C.1: Single degree of freedom system

The response $x(t)$ under a general force excitation $F(t)$ is given by the Duhamel's integral:

$$x(t) = \int_{-\infty}^{+\infty} F(\tau)h(t-\tau)d\tau \tag{C.1}$$

where $h(t)$ represents the impulse-response function,i.e. the system's response to an excitation with an impulse of unity, $F(\tau) = I\delta(\tau)$ with $I = 1$ (δ is the Dirac function). By changing the variable from τ to $\theta = t - \tau$, the previous equation is rewritten as:

$$x(t) = \int_{-\infty}^{+\infty} F(t-\theta)h(\theta)d\theta \tag{C.2}$$

Since the excitation is a stationary Gaussian process, then for a linear system the response is also a stationary Gaussian process [59] and thus the auto-correlation function of the response signal $x(t)$ is found by:

$$\begin{aligned} R_x(\tau) = E[x(t)x(t+\tau)] &= \mathrm{E}\left[\int_{-\infty}^{+\infty} F(t-\theta_1)h(\theta_1)d\theta_1 \int_{-\infty}^{+\infty} F(t+\tau-\theta_2)h(\theta_2)d\theta_2\right] \\ &= \int_{-\infty}^{+\infty}\int_{-\infty}^{+\infty} \mathrm{E}[F(t-\theta_1)F(t+\tau-\theta_2)h(\theta_1)h(\theta_2)d\theta_1 d\theta_2] \\ &= \int_{-\infty}^{+\infty}\int_{-\infty}^{+\infty} R_F(\tau+\theta_1-\theta_2)h(\theta_1)h(\theta_2)d\theta_1 d\theta_2 \end{aligned} \tag{C.3}$$

The power spectral density of the response is defined by the Wiener-Khintchine relation as:

$$S_x(\omega) = \frac{1}{2\pi}\int_{-\infty}^{+\infty} R_x(\tau)e^{-i\omega\tau}d\tau \tag{C.4}$$

Applying Equation C.3 into C.4 gives:

$$\begin{aligned} S_x(\omega) &= \frac{1}{2\pi}\int_{-\infty}^{+\infty} e^{-i\omega\tau}d\tau \cdot \int_{-\infty}^{+\infty}\int_{-\infty}^{+\infty} R_F(\tau+\theta_1-\theta_2)h(\theta_1)h(\theta_2)d\theta_1 d\theta_2 \\ &= \int_{-\infty}^{+\infty} h(\theta_1)e^{i\omega\theta_1}d\theta_1 \int_{-\infty}^{+\infty} h(\theta_2)e^{-i\omega\theta_2}d\theta_2 \\ &\cdot \frac{1}{2\pi}\int_{-\infty}^{+\infty} R_F(\tau+\theta_1-\theta_2)e^{-i\omega(\tau+\theta_1-\theta_2)}d\tau \\ &= H^*(\omega)H(\omega)\cdot\int_{-\infty}^{+\infty} R_F(\tau+\theta_1-\theta_2)e^{-i\omega(\tau+\theta_1-\theta_2)}d\tau \end{aligned} \tag{C.5}$$

where $H(\omega)$ is the system's complex frequency response function (FRF), given by the direct Fourier transformation of the impulse-response function $h(t)$, and $H^*(\omega)$ is the complex conjugate of $H(\omega)$. Finally, by introducing the variable $\eta = \tau + \theta_1 - \theta_2$, Equation C.5 gives:

$$S_x(\omega) = |H(\omega)|^2 S_F(\omega) \tag{C.6}$$